Analytical approach to crack tip plasticity of dental CoCrMo alloy

Lovrenić-Jugović, Martina; Slokar Benić, Ljerka; Jandrlić, Ivan

Source / Izvornik: **Machines, Technologies, Materials, 2022, 16, 248 - 250**

Journal article, Published version
Rad u časopisu, Objavljena verzija rada (izdavačev PDF)

Permanent link / Trajna poveznica: https://urn.nsk.hr/urn:nbn:hr:115:581827

International journal
for science, technics and
innovations for the industry

MACHINES TECHNOLOGIES MATERIALS

YEAR XVI Issue 7 / 2022 ISSN PRINT 1313-0226
ISSN WEB 1314-507X

Published by
Scientific technical
Union of Mechanical Engineering

MACHINES. TECHNOLOGIES. MATERIALS

INTERNATIONAL SCIENTIFIC JOURNAL

ISSN PRINT 1313-0226, ISSN WEB 1314-507X, YEAR XVI, ISSUE 7 / 2022

Scientific and technical union of mechanical engineering
108 R. S. Rakovski str., Sofia, Bulgaria
www.stumejournals.com, office@stumejournals.com

C O N T E N T S

MACHINES

Dependance on the required power of the electric motor on the CNC Spinner EL-510 lathe according to the depth of cut for turning and facing with CNMG 120408-PM 4325 tool insert
Violeta Krcheva, Marija Chekerovska 228

TECHNOLOGIES

Study on the influence of cutting fluid on flat grinding process
Badea Lepadatescu, Flavia Fechete 231

The influence of tool path strategies for 3- and 5-axis milling on the accuracy and roughness of shaped surfaces
Peter Ižol, Zuzana Grešová, Marek Vrabeľ, Jozef Brindza, Michal Demko 234

Disposal of Spent Ionizing Radiation Sources Cobalt-60
Ulugbek Ashrapov, Ilkham Sadikov, Bakhodir Mirzaev, Shavkat Malikov, Valery Nesterov 238

Investigation of the interface of two-layer diamond plates for drilling tools
Viacheslav Prokhorov, Sergey Perfilov, Anrey Pozdnyakov 241

MATERIALS

About corrosion damage of the railway wheels
Svetlana Gubenko 243

Analytical approach to crack tip plasticity of dental CoCrMo alloy
Martina Lovrenić-Jugović, Ljerka Slokar Benić, Ivan Jandrlić 248

Nanophase structures in vacuum multilayer coatings formed on tool and high-speed steels
Yauheni Auchynnikau, Nikolai Chekan, Gennady Kostukovich, Igor Akula, Alexander Ogorodnikov A. 251

Features of the tribological behavior of the magnesium alloy Mg -1% ca depending on the structural state
Vladimir I. Semenov, Hsin-Chih Lin, Sergey V. Chertovskikh, Olga B. Kulyasova 255

Recent developments and regulations in fire resistance of wood and wood-based composites
Nadir Ayrilmis 260

Dependance on the required power of the electric motor on the CNC Spinner EL-510 lathe according to the depth of cut for turning and facing with CNMG 120408-PM 4325 tool insert

Violeta Krcheva[1], Marija Chekerovska[1]
[1]Faculty of Mechanical Engineering
'Goce Delcev' University - Stip, Republic of North Macedonia
violeta.krceva@ugd.edu.mk, marija.cekerovska@ugd.edu.mk

Abstract: *A lathe is a machine that removes metal from a workpiece to the required shape and size. A lathe operates on the principle of a rotating workpiece and a fixed cutting tool. The cutting tool is fed into the workpiece, which rotates about its own axis, causing the workpiece to be formed into the desired shape. The operation by which the excess material is removed from the workpiece to produce a cone or cylindrical shape is called turning, and the operation used to cut a flat surface perpendicular to the workpiece's rotational axis is called facing. Speed, feed, and depth of cut are important factors that have to be determined according to the power of the CNC Spinner EL-510 lathe using a PCLNR 2525M 12 shank tool and a CNMG 120408-PM 4325 tool insert.*
Keywords*: MACHINING, METAL CUTTING, CUTTING CONDITIONS, SPEED, FEED*

1. Introduction

The material removal processes are a family of shaping operations in which the removal of material from a starting workpiece results in a transformed product machined to the desired final geometry. The most important branch of that family is machining. Machining, as a manufacturing process, is most frequently applied to shape metals into convenient products, which consists of forcing a sharp cutting tool to cut away a layer of material on the workpiece blank to achieve the desired part shape and size. Actually, machining is a generic term, applied to all material removal, while metal cutting refers to processes in which the excess material is removed by a harder tool, through a process of extensive plastic deformation or controlled fracture [1].

The predominant cutting action in metal cutting involves separation of the work material to form a chip. When the cutting tool is fed along the finished contour, a new surface is generated. It is usually performed after other manufacturing processes that create the general shape of the starting workpiece, and metal cutting provides the final geometry of the resulting work surface. Metal cutting is important in the process of manufacturing (commercially and technologically) as a consequence of applying a variety of work materials for different part shapes (with regular and irregular geometry features), achieving dimensions to very close tolerances with appropriate smooth surface finishes.

In fact, metal cutting is not just an individual specific process - it is a group of certain processes. The common feature is the aim of generating the shape of the workpiece using a sharp cutting tool of harder material to form a final workpiece with precise dimensions or to improve the tolerances and quality of the surface finish of an already produced workpiece. To realize the metal cutting operations, relative motion is required between the workpiece and the cutting tool. The relative motion is performed (in most operations) by a primary and a secondary motion. The primary motion (called the cutting speed) is attained with the spinning of the workpiece, and the secondary motion (called the feed) is obtained by the linear movement of the cutting tool (Fig. 1(a)).

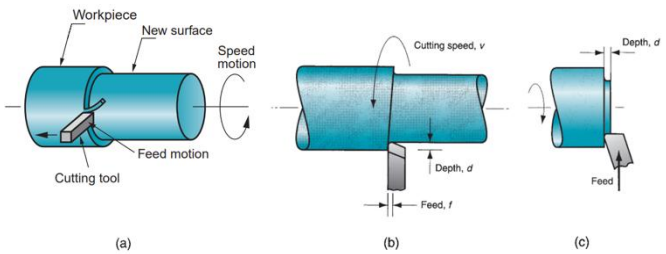

Fig. 1 *(a) Creating a shape in metal cutting by turning, (b) Turning cutting conditions, and (c) Facing cutting conditions*

Conclusively, the primary motion is accomplished at a certain cutting speed (*v*). In addition, the tool must be moved laterally across the work. This is a much slower motion, called the feed (*f*). The remaining dimension of the cut is the penetration of the cutting tool below the original work surface, called the depth of cut (*d*). Collectively, speed, feed, and depth of cut are called the cutting conditions [2].

Here are discussed cutting conditions for turning and facing (as one of the most common types of metal cutting) in more detail.

In turning, the workpiece revolves around its central axis. The cutting tool moves along the axis of rotation at a constant speed, removing excess material to form a cylinder, cone, or surface with a more complex profile. The rotating workpiece performs the speed motion, and the cutting tool achieves the feed motion by moving at a slow pace in a direction that is parallel to the workpiece's axis of rotation. In facing, the perpendicular movement of the cutting tool to the axis of rotation of the workpiece removes excess material from the workpiece's end and/or shoulder to create a new smooth surface. The cutting conditions for turning and facing are illustrated in Figure 1(b) and Figure 1(c), respectively. A typical unit used for cutting speed is [m/min], for feed is [mm/rev] and for depth of cut is [mm].

The cutting conditions in turning and facing generally incorporate the speed motion combined with a feeding motion and depth of cut to create the correct shape of the workpiece by the geometry of the cutting tool and its penetration into the work surface. The cutting tool has just one or even more sharp cutting edges. It is made of a material harder than the workpiece material. The purpose of the cutting edges is to separate a chip from the current workpiece in order to generate a new surface.

The surface of the tool over which the chip flows is known as the rake face. The cutting edge is formed by the intersection of the rake face with the clearance face or flank of the tool. The rake angle is measured from a line parallel to the axis of rotation of the workpiece. A positive rake angle is one where the rake face dips below the line, but the greater robustness of tools with a smaller rake angle leads in many cases to the use of a zero or negative rake angle. The tool terminates in an end clearance face, which is also inclined at such an angle as to avoid rubbing against the freshly cut surface. The nose of the tool is at the intersection of all three faces and may be sharp, but more frequently there is a nose radius between the two clearance faces [3].

Performing the operation with a positioned cutting tool relative to the workpiece requires a compatible machine tool. A machine tool, as a term, is applied to any power-driven machine that realizes a machining operation. It also indicates metal forming and metal

cutting processes. The requirement of the machine tool is to provide power for the operation at the determined speed, feed, and depth of cut related to the rotating workpiece and the movement of the cutting tool. The traditional machine tools used to implement the process of turning and facing are lathes. Instead of controlling the tool machine and the operation by a human operator who changes the cutting tool and sets the cutting conditions, a modern form of control (as a form of automation) is computer numerical control (CNC), in which the operation is controlled by a program of instructions. Despite the particular operation and the level of control, appropriate power is required to accomplish the activities in order to perform the exact operation.

2. Research

The purpose of this research is to determine how the required power of the electric motor on the CNC Spinner EL-510 lathe (with a maximum power of the main motor of 13,4[kW] and a mechanical efficiency of 80%) affect turning and facing operations when the work material, cutting tool, and cutting conditions are identical. The specified work material is C1430 (corresponding to the JUS C.B9.021 Standard for Heat - treatable Steels) with a hardness of 172 HB. The applied cutting tool is a combination of a CNMG 120408-PM 4325 indexable insert mechanically clamped into a PCLNR 2525M 12 shank tool (see Fig. 2). The cutting tool has the following elements of geometry: an approach (or cutting edge) angle of 95º, an entering (or lead) angle of -5º, an orthogonal rake angle of -6º, a clearance angle of 0º, and a corner radius of 0,8[mm].

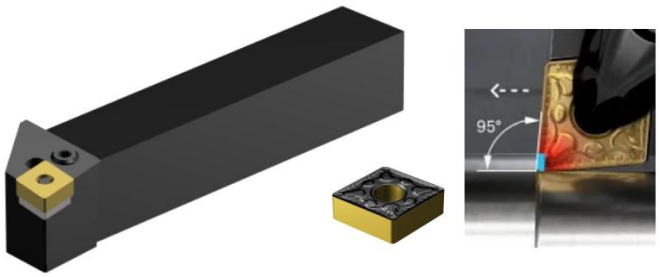

Fig. 2 *The Cutting Tool*

The corresponding grade number of surface roughness to the geometric tool factors is N10, and the appropriate value for the average roughness is 3,2 [μm]. The chosen cutting feed to achieve the defined surface quality is 0,83 [mm/rev]. The depth of cut is from 0,5 [mm] to 3 [mm] and it changes every 0,5 [mm] in order to calculate the essential motor power for turning and facing operations. The proper cutting speed is 180 [m/min] up to 1 [mm] depth of cut, and as the depth of cut increases from 1÷3 [mm], the cutting speed decreases to 140 [m/min].

The power required to operate the machine tool is greater than the power delivered to the cutting process because of mechanical losses in the motor and drive train in the machine [4].

The total product of the depth of cut, cutting speed, feed and the specific power coefficient for a particular operation gives the power required to perform the turning operation, while half the product gives the power required to perform the facing operation.

For turning:

(1) $$P_R = d \cdot v \cdot f \cdot p$$

where P_R is the power required to perform the turning operation, d - depth of cut, v - cutting speed, f – feed, p - specific power coefficient for a particular operation.

For facing:

(2) $$P_R = \frac{d \cdot v \cdot f \cdot p}{2}$$

where P_R is the power required to perform the facing operation, d - depth of cut, v - cutting speed, f – feed, p - specific power coefficient for a particular operation.

As a result of mechanical losses in the motor and drive train in the machine, the total required power is greater than the required power to perform the operation, and these types of losses can be estimated with the mechanical efficiency of the lathe:

(3) $$P = \frac{P_R}{E}$$

where P is the total required power, P_R - power required to perform the operation, E - mechanical efficiency of the lathe.

3. Results and discussion

Considering the specified work material, cutting tool, cutting conditions, and mechanical efficiency of the lathe, Table 1 lists (and Fig. 3 shows) the required power to perform turning and facing operations.

Table 1: *Required power for turning and facing operations*

d [mm]	0,5	1	1,5	2	2,5	3
f[mm/rev]	0,83	0,83	0,83	0,83	0,83	0,83
v[m/min]	180	180	140	140	140	140
P_R [kW] – Turning	4,78	9,56	11,16	14,87	18,59	22,31
P[kW] – Turning	**5,98**	**11,95**	**13,95**	**18,59**	**23,24**	**27,89**
P_R [kW] – Facing	2,39	4,78	5,58	7,44	9,3	11,16
P[kW] – Facing	**2,99**	**5,98**	**6,98**	**9,3**	**11,63**	**13,95**

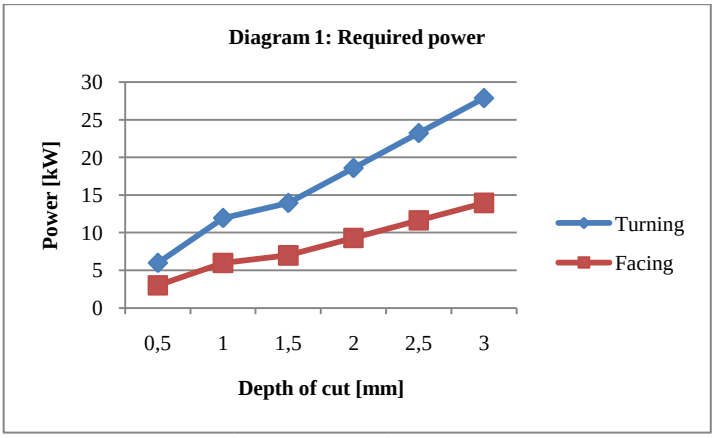

Fig. 3 *Required power for turning and facing operations on the CNC Spinner EL-510 lathe*

Turning and facing, as different types of metal cutting processes, require various values of motor power to perform the removal of a unit volume of metal during the process. Using this measure, turning and facing can be compared in terms of power requirements for identical work material, cutting tool and cutting conditions. The required power to accomplish a particular turning and facing operation (considering the results presented in Table 1 and Diagram 1) depends on the value of the depth of cut.

With the intention of increasing depth of cut, increasing motor power is required in performing these operations. The essential motor power is different in the two cases.

Considering that turning is a process of material removal with a cutting tool parallel to the rotation axis of the workpiece and facing is a process of material removal with a cutting tool perpendicular to the rotation axis of the workpiece, with turning the diameter of material is removed and with facing the length of material is removed.

The turning operation reduces the diameter of the workpiece from its original diameter to a final diameter, also known as the depth of cut. Actually, the depth of cut is the radius of the workpiece around which excess material is removed.

The total removed material during the process of turning is the sum of the two radiuses, i.e., it is a process of removing material from both sides of the workpiece, which results in a duplicated value of the depth of cut. On the other hand, in a facing operation, the cutting tool moves from the outer diameter of the workpiece towards the center (or inner diameter), removing a single value of the depth of cut.

Therefore, the power required to perform the turning process is two times higher than the power required to perform the facing process.

4. Conclusion

For the specified CNC Spinner EL-510 lathe's motor power of 13,4 [kW], it is recommended to perform turning up to a maximum of 1 [mm] and facing up to a maximum of 2,5 [mm] depth of cut. It is important to emphasize that to complete turning and facing operations in the same circumstances for higher values of the depth of cut, it is crucial to apply a higher power rating electric motor.

5. References

[1] Schey, J. A. *Introduction to Manufacturing Processes*, 2nd ed., McGraw Hill, Singapore, 1987, pp.442

[2] Groover, M. P. *Fundamentals of Modern Manufacturing: Materials, Processes, and Systems*, 4th ed., John Wiley & Sons, United States of America, 2010, pp.487

[3] Trent, E., and Wright, P., *Metal Cutting*, 4th ed., Butterworth–Heinemann, United States of America, 2000, pp. 11

[4] Groover, M. P. *Fundamentals of Modern Manufacturing: Materials, Processes, and Systems*, 4th ed., John Wiley & Sons, United States of America, 2010, pp.498

[5] Kaushish, J. P. *Manufacturing Processes*, 2nd ed., PHI Learning, New Delhi, 2010

[6] Ostwald, P. F., and Munoz, J. *Manufacturing Processes and Systems*, 9th ed., Wiley India, New Delhi, 1997

[7] Cvetkov, S. *Metal cutting and plastic deformation*, Goce Delcev University, Stip, 2014 [In Macedonian]

[8] Cvetkov, S. *Practicum for metal cutting and plastic deformation*, Goce Delcev University, Stip, 2015 [In Macedonian]

Study on the influence of cutting fluid on flat grinding process

Badea Lepadatescu, Flavia Fechete
Transylvania University of Brasov
Romania
lepadatescu@unitbv.ro, flavia.fechete@unitbv.ro

***Abstract**: In the paper is presented a study regarding the influence of different factors on the roughness of machined surfaces obtained by manufacturing process of flat grinding. The workpieces that were used on the experimental tests were radial bearing ring with needles made of steel hardened to 60-64 HRC. It were taken into consideration factors like, the size of the machined surface, the traverse speed, the grain size of abrasive grinding wheels, cutting fluid.*
During the experiments was used the method of the Box-plot graphical representation that aims to observe and characterize the distribution of values obtained on these tests.
***Keywords:**GRINDING PROCESS, CUTTING FLUID, SURFACE FINISH*

1. Introduction

Simultaneous flat grinding is a process of flat grinding in which the parts are machined simultaneously on both sides of the front of the abrasive bodies. The machining process has a high productivity, so these types of machines can not operate without automatic feeding systems and discharge of machined parts.
The machined parts are pushed into the grinding slot by a roller drive system and are guided by two linear supports. The two abrasive discs can be mounted with horizontal (Fig.1.a) or vertical axes (Fig.1b).

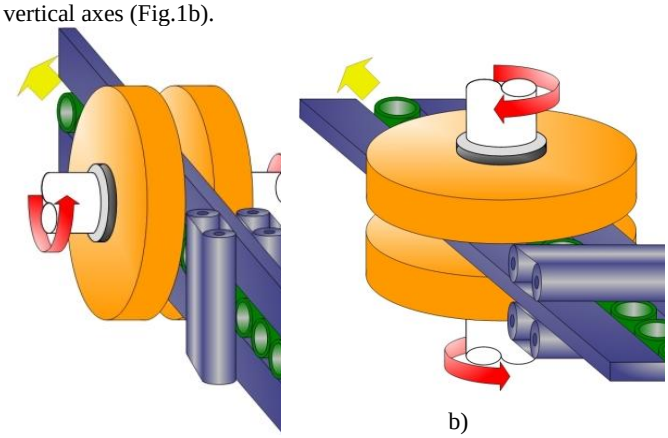

a) b)

***Fig.1** Principle of operation of simultaneous flat grinding machines. a) Abrasive bodies with horizontal axes; b) Abrasive bodies with vertical axes.*

In the following we will refer only to the process of simultaneous flat grinding of the needle bearing rings (Fig.2), made of steel hardened to 60-64 HRC. The amount of material removed from workpiece faces depends on the speed of the abrasive wheels.
If asymmetrical parts are machined (ex. tapered roller bearing rings), in order to remove the same material from both sides, it is necessary to respect the relation (1):

$$\frac{n_1}{n_2} = \frac{S_1}{S_2} \qquad (1)$$

where S_1, S_2 represent the areas of the two flat surfaces of the part which are machined simultaneously, and n_1, n_2 - the rotations of the two abrasive wheels which simultaneously cut the flat surfaces of the areas S_1 and S_2 respectively [1].

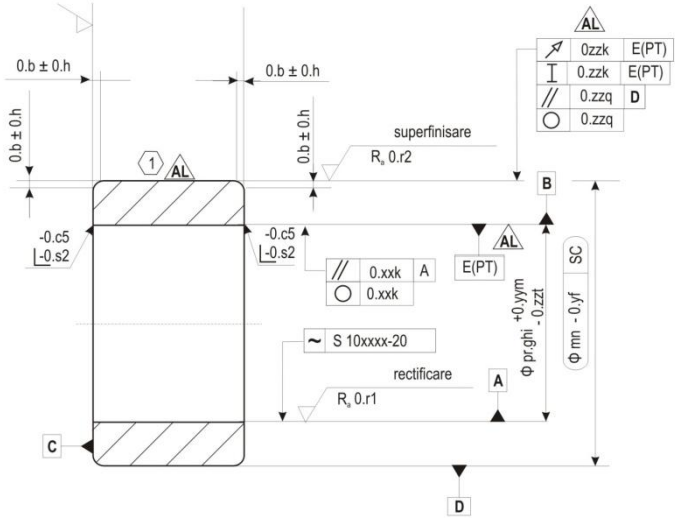

***Fig.2** Radial bearing ring with needles.*

2. Analysis of simultaneous flat grinding process performance

During the experiments the population was considered to consist of all the parts processed between two successive dressings of the abrasive wheels (around 40,000 pieces). Due to the large number of parts, not all of them can be measured. A sample was taken from the population: 5 pieces for every 5000 pieces. Next, the R_a and R_z roughness on both sides of the workpiece surfaces were measured. We will note with R_{amax} and R_{zmax} the highest value obtained by measuring R_a and R_z on both side of the machined parts.

It is found that the R_a roughness values decrease immediately after dressing abrasive wheels, and then remain constants. When the grinding wheels have worn out, the abrasive grains no longer cut but "break" the metal from the part. In this way the roughness of the parts increases rapidly[4]. The dispersion of the 55 measured values of R_{amax} roughness is represented in Fig.3. Note that the standard deviation is 0.003 and the arithmetic mean is 0.334.

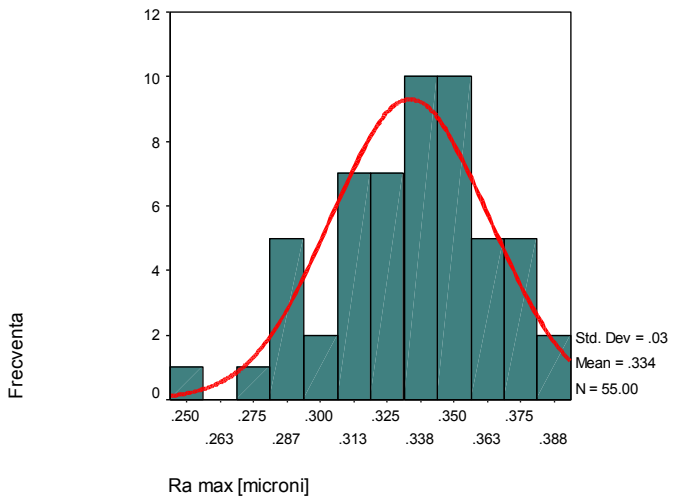

Fig.3 *Dispersion of roughness R_{amax} for parts between two dressings.*

3. The influence of the size of the machined surface on part roughness

In the following we will note with R_{AMIN17} and R_{AMAX17}, R_{AMIN18} and R_{AMAX18} , R_{AMIN19} and R_{AMAX19} respectively the roughness R_a measured on both sides of parts with diameter of 17 mm, 18 mm and 19 mm diameter [2]. The large number of measurements is observed (60 pieces for pieces with diameter of 17 mm and 19 mm respectively and 55 pieces for pieces with diameter of 18 mm) in order to draw conclusions with a high degree of generality.

Table 1 Descriptive statistics indicators

	N		Mean		Std. Deviation	Variance	Range	Minimum	Maximum
	Valid	Missing							
	Statistic	Statistic	Statistic	Std. Error	Statistic	Statistic	Statistic	Statistic	Statistic
RAMIN17	60	0	.27512	3.53E-03	2.73E-02	7.48E-04	.141	.226	.367
RAMAX17	60	0	.30755	4.45E-03	3.45E-02	1.19E-03	.170	.247	.417
RAMIN18	55	5	.30020	3.61E-03	2.68E-02	7.17E-04	.136	.217	.353
RAMAX18	55	5	.33385	3.98E-03	2.95E-02	8.71E-04	.136	.256	.392
RAMIN19	60	0	.29882	4.17E-03	3.23E-02	1.04E-03	.158	.214	.372
RAMAX19	60	0	.33323	4.20E-03	3.25E-02	1.06E-03	.163	.273	.436

The amplitude of the dispersions is between 0.136µm and 0.170µm.

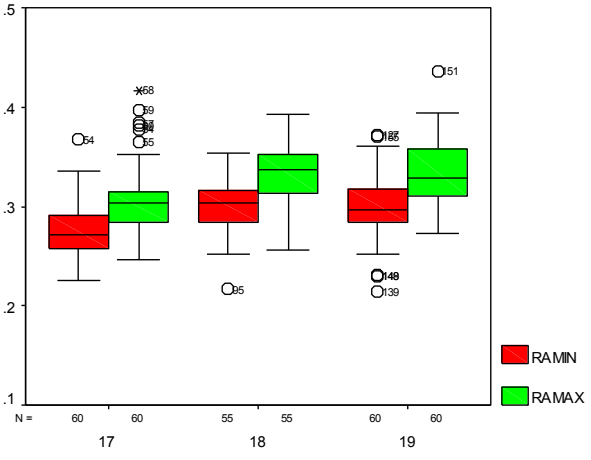

Fig.4 Box plot R_a for parts of diameter 17, 18, 19 mm.

From the analysis of Fig.4 is found that the size of the machined surface does not greatly influence the roughness of the machined surfaces [3].

4. The influence of the traverse speed on the part roughness

The same principle of population sampling was applied: 5 pieces were taken for every 5000 pieces processed. R_a roughness was measured on both sides and R_{amin} and R_{amax} values were obtained.

Table 2 Descriptive statistics indicators

	N		Mean		Median	Std. Deviation	Variance	Range	Minimum	Maximum
	Valid	Missing								
	Statistic	Statistic	Statistic	Std. Error	Statistic	Statistic	Statistic	Statistic	Statistic	Statistic
RAMIN8.1	35	70	.29569	6.98E-03	.29600	4.13E-02	1.70E-03	.178	.212	.390
RAMAX8.1	35	70	.33146	7.66E-03	.32800	4.53E-02	2.06E-03	.184	.242	.426
RAMIN8.7	30	75	.26010	5.77E-03	.25700	3.16E-02	9.99E-04	.138	.179	.317
RAMAX8.7	30	75	.28950	6.24E-03	.28450	3.42E-02	1.17E-03	.144	.211	.355
RAMIN9	40	65	.32860	8.03E-03	.32900	5.08E-02	2.58E-03	.213	.226	.439
RAMAX9	40	65	.36645	9.43E-03	.36400	5.97E-02	3.56E-03	.214	.253	.467

As expected, the increase of part's feed rate, led to a certain increase in the roughness of R_a and to an increase of spreading values obtained.

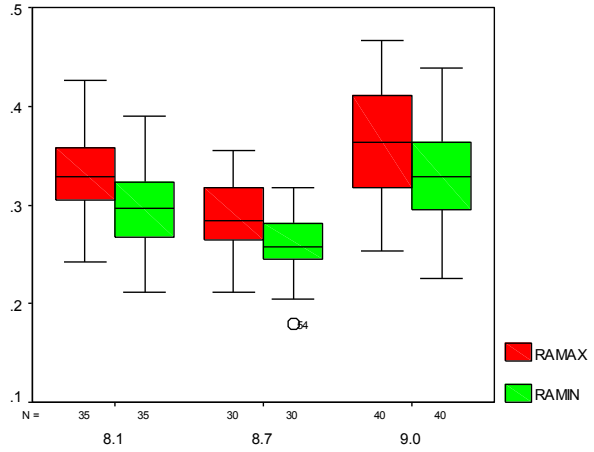

Fig.5 *Box-plot R_a depending on the feed rate of the parts.*

From the analysis of the dispersions represented in Fig.5 it is observed that the largest width is presented by the "box" obtained for the roughness of the pieces with diameter of 19mm.
In this case, the large number of measurements performed is noticeable: 35, 30, respectively 40, in order to obtain information with a high degree of certainty[6].

5. The influence of the grain size of abrasive grinding wheels on the machined parts roughness

Fig.6 and Fig.7 show the Box-plots of the roughness's R_a and R_z for the machined parts with abrasive wheels of different grain sizes.

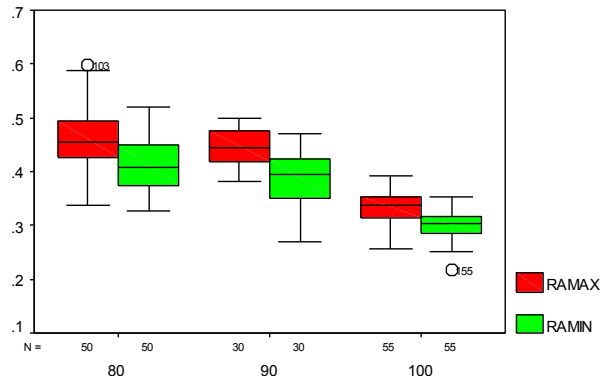

Fig.6 *Box-plot R_a roughness depending on abrasive grain size.*

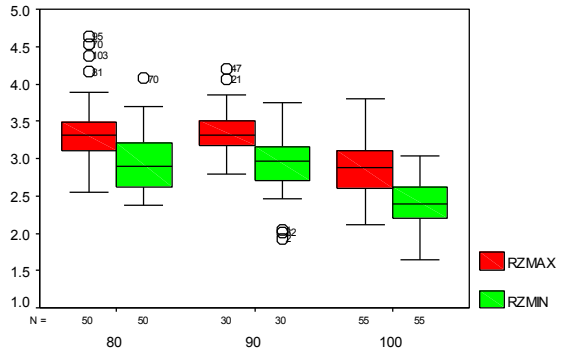

Fig.7 *Box-plot R_z roughness depending on abrasive grain size.*

Except for the abrasive wheels, the other cutting conditions were kept constant. It is found that as the grain size of the abrasive wheels is finer, the roughness Ra of the machined surfaces decreases accordingly [5].

6. The influence of the cutting fluid on the roughness of the machined parts

The roughness R_a and R_z of the parts were measured before and after changing the cutting fluid, using the same experimental design (after each 5000 machined parts, 5 pieces were measured).

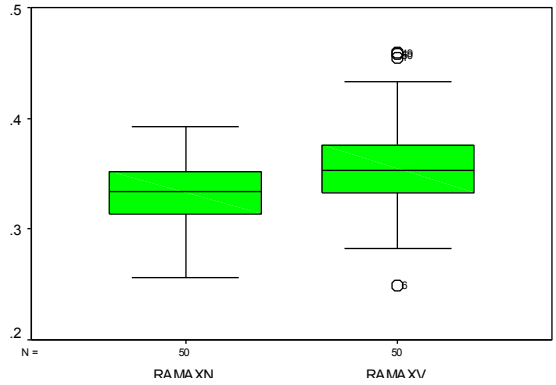

Fig.8 *Box - plot R_{qmax} for old and new cutting fluid used.*

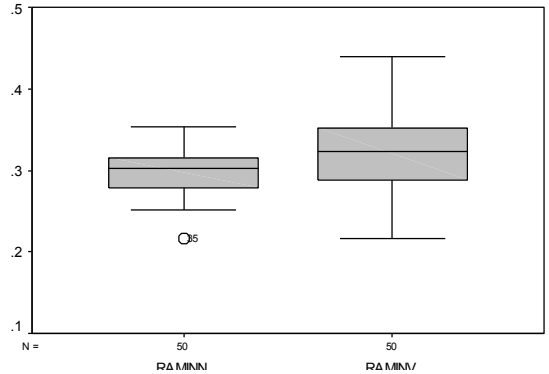

Fig. 9 *Box - plot R_{amin} for old and new cutting fluid used.*

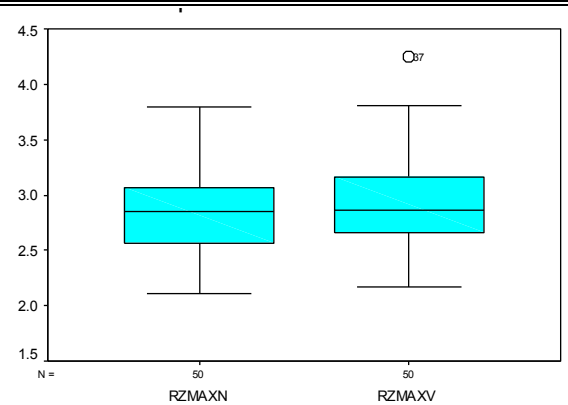

Fig.10 *Box - plot R_{zmax} for old and new cutting fluid used.*

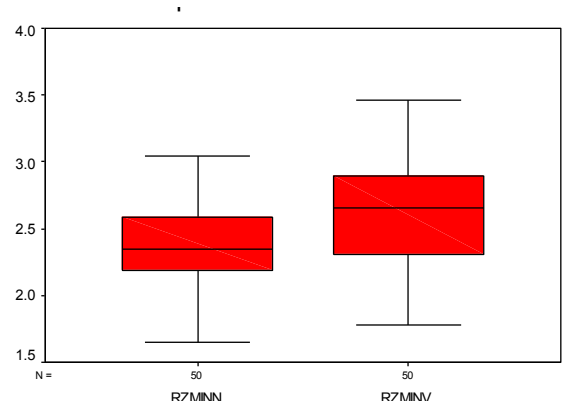

Fig.11 *Box - plot R_{zmin} for old and new cutting fluid used.*

7. Conclusions

1. The size of the machined surface, characterized by the variable diameter: 17mm, 18mm, 19mm (all parts have the same inner diameter) does not significantly influence the R_{amin} and R_{amax} roughness of the machined parts;
2. The traverse speed of the parts (8m / min, 8.7 m / min, 9m / min, 11m / min) does not have a great influence on the quality of the machined surfaces;
3. The size of the grain size of abrasive wheels greatly influences the quality of the machined surface. The larger the grain size, the higher the roughness of the machined parts. This is proof that the roughness of machined parts is the result of the overlapping marks left by the abrasive grains on the surface of the part.
4. The quality of the cutting fluid does not greatly affect the roughness of the machined parts. This is due to the stability of the machine tool-tooling system and the strict observance of proper cutting fluid management.

8. References:

[1] Awiszus, B., Matthes, K-J., Duerr, H., Bast, J. –Grundlagen der Fertigugstechnik, Seiten 125-130, Editura Hanser, 2006
[2] Beyer, P. –Hochproduktive Vit- CBN- Schleifwerkzeuge, *in SMM Fertigungstechnick, Nr.4- 2005, Seiten 60- 63.*
[3] Bock, R: Vorlesung Fertigungstechnick, Übung Zeitspanunsvolumen, Juni 2006
[4] K.D. Bouzakis, C. Karachaliou: Process Models in grinding, based on three dimensional description of the grinding wheel topomorphy, North American Manufacturing Research Conference Proceedings, May 19-22, 1985
[5] Brinksmeier, H., Koch, T. –Auswirkungen des mikrobiellen befalls von wassermischten Kühlschmierstoffen auf das Zerspanergebnis , Presentation bei Resourceshonende Metallbearbetung, Arbeitkreis Kuehlschmierstoffe, IWT, Bremen, Sept.2002
[6] Kleber, M. –Kuehlschmierstoffe: Analytisch-chemische Charakterisierung und Untersuchungen zur mutagenen Wirkung, *Inaugural- Dissertation zur Erlangung des Doktorgrades der Naturwissenschaften, Dortmund, 2000, Seiten 5- 20*

The influence of tool path strategies for 3- and 5-axis milling on the accuracy and roughness of shaped surfaces

Peter Ižol, Zuzana Grešová, Marek Vrabeľ, Jozef Brindza, Michal Demko
Faculty of Mechanical Enginering, Technical University of Košice, Slovakia
E-mail: peter.izol@tuke.sk, ingzgresova@gmail.com, marek.vrabel@tuke.sk, jozef.brindza@tuke.sk, michal.demko@tuke.sk

Abstract: *Free form or shaped surfaces are found on a large number of modern engineering products. 3- or multi-axis CNC milling is usually used in their production. CAM systems are almost exclusively used in the creation of control programs. The aim of the presented research was to compare the quality of shaped surfaces made by 3- and 5-axis milling using three frequently used strategies. A sample with hemispherical surfaces was designed for the experiment. The surfaces predicted by the CAM system were compared with the surfaces actually produced. The disagreement of the predicted surface deviations with the deviations of the produced surfaces was demonstrated. In the evaluation of surface roughness, the advantage of 5-axis milling was partially demonstrated when one of the strategies achieved lower roughness, at two strategies the roughness was identical to 3-axis milling.*
KEYWORDS: *CNC MACHINE-TOOL, FREE FORM SURFACES, MILLING STRATEGIES, SURFACE QUALITY*

1. Introduction

The requirement to produce increasingly complex parts with better quality requires the use of efficient production processes. Product diversity increases and seriality decreases, which complicates process standardization and the use of known technological settings. Shaped surfaces occur on an increasing number of engineering products, and CNC milling is considered to be the most productive and flexible method for manufacturing such surfaces.

3- or 5-axis milling machines are most often used in the production of parts with shaped surfaces. the decision to use a 3- or 5-axis milling machine is not simple. Decides the complexity and required accuracy of parts, operating costs of machines, their productivity, knowledge and, last but not least, the experience of CNC programmers and machine operators [1]. In general, the following applies to the use of a 5-axis machine:

- production time is shortened because one clamping and one zero point are used instead of several clamps and individual zero points for each clamping,
- the accuracy of the parts is higher, because in 3-axis milling, every loosening and clamping has an adverse effect on the accuracy.

But the use of 5-axis machines also has its drawbacks:

- the machine price and production costs are higher than with a 3-axis machine,
- staff with a higher level of education and experience are needed, whether they are programmers or operators,
- programming and supplementary systems (CAM system, post processors) are more expensive, the cost of training people is necessary.

Reference [2] points out the differences between the shaped surfaces made by 3-axis, 3 + 2-axis and 5-axis milling. Lists the advantages of 5-axis milling over 3 + 2-axis milling, which include increased milling accuracy, shortened cutting time, extended tool life, improved functional properties of the machined surface, reduced cutting forces, and more. When comparing the machining accuracy of 3-axis, 3 + 2-axis and 5-axis milling, the highest accuracy was achieved in 5-axis milling. 3 + 2-axis milling shows more favourable surface roughness values. CAM prediction of residual material corresponded most to the actually measured residual material in 5-axis milling. The results are valid for the CAM system used. Similar comparisons indicate the quality of the computational algorithm used in the CAM system.

Sadílek et al. [3] compares 3-axis and 5-axis milling in making some basic geometric shapes. It is stated that both milling methods achieve almost the same shape deviations. However, the deviations achieved by 5-axis milling were smaller with a better quality of the machined surface.

Stejskal et al. [4] describes a method for optimizing the orientation of tool axes in multi-axis milling. the toolpath is optimized to achieve a more constant cutting speed, which leads to improved surface quality and increased productivity. However, the authors state that the position of the tool is limited by the shape of the machined surface, the kinematics of the machine and the shape of the machined part due to possible collisions. Therefore, it is not always possible to achieve the ideal value of the contact diameter of the tool on the entire machined surface.

The mathematical model for predicting the roughness of the milled surface is defined in [5], the model for ensuring a constant scallop height is described in [6]. Kolar et al. [7] describes a virtual model of the machine, which can be used not only in simulations of the milling process but also for accurate determination of the milling time and surface condition after machining. The model allows to influence the accuracy, quality and productivity of machining by setting the interpolator.

Deviations from the required shapes or dimensions are caused by machine errors, incorrect clamping or deformation of the workpiece and incorrect clamping of the tool, etc. Surface roughness is one of the primary requirements in the design of engineering products. It is a widely used product quality indicator and is usually measured off-line when the component has already been machined [8]. The quality of the milled surface also depends on various technological parameters such as cutting conditions or the properties of the coolants. The source presents a series of mathematical models for determining the surface roughness for commonly used shape milling methods (vertical, push, pull, oblique, oblique push and oblique pull) and determines the effect of the milling method used on the resulting surface roughness in ball-nose end milling.

Machining of shaped surfaces is generally associated with the concept of machining strategy. The milling strategy used depends on the relative position of the cutting tool and the workpiece, as well as the kinematics of the cutting tool during the operation. Strategies must meet increasing requirements for accuracy and surface integrity, shortening cutting times or reducing cutting forces.

Bagci et al. [9] defines a simulation and optimization system based on body modelling, integrated with a CAD/CAM system. Experimental results show the impact of milling strategies on cutting time and their importance for shortening production time and reducing costs. Strategies also affect tool deflection, material removal rate values, cutting forces, and cutting errors.

The use of different strategies in ball end milling on low-curvature convex surfaces has a significant impact on cutting forces, surface texture, and machining time [10]. Radial paths provide good results in terms of a more even surface structure and lower cutting forces but have the highest machining time. Cutting forces are highest when using a spiral strategy due to the contact area between the tool and the material. Overall, the use of a spiral toolpath strategy to finish milling these types of surfaces is not recommended.

Mali et al. [11] examines three strategies - linear, linear rotated by 90°, and offset. 3D offset is the best finishing strategy because it ensures uninterrupted tool work, which is favourable for milling. The tool life is increased and a better surface condition is achieved. The active cutting speed and the position of the contact surface are important parameters that control the chip removal

mechanism, affect the cutting forces, and the overall surface quality of the shaped surfaces.

The influence of strategies on surface roughness in the application of dies and molds is addressed in [12]. The path strategy influences real machining time, polishing time and costs. When comparing several strategies, the best results were achieved by 3D offset and spiral which slice the part in a horizontal manner.

Ramos et al. [13] compares three typical milling strategies, namely radial, raster, and 3D offset. Their effect on surface roughness, texture, and dimensional deviations was evaluated. Even in this case, the 3D offset strategy proved to be the most suitable. However, as the authors state, the results cannot be generalized. The study provides a general trend in machining surfaces similar to those tested.

Logins et al. [14] evaluates three strategies of high-speed milling, namely linear, linear in two perpendicular directions and circular. surface roughness and texture were evaluated parameters. To achieve the lowest possible surface roughness, a linear path is recommended, the most even surface structure is provided by a circular strategy. The authors recommend avoiding a linear strategy in two perpendicular directions, and also emphasize that the results depend on the material being machined.

Sales et al. [15] evaluates eight finishing strategies for 3- and 5-axis milling in terms of machining time and the average residual load per unit area. The comparison was performed with NC codes directly from the CAM system and NC codes modified by the optimization software. The authors determined the best strategies for specific types of surfaces and at the same time showed that the feed optimization balances the machining times of different strategies. By optimizing the feed rate, the machining time is reduced by 20 to 50%.

2. Descriptions of experiments

The aim of the experiments was to compare 3-axis and 5-axis milling using 3 different strategies commonly used in the production of components with shaped surfaces. The following steps have been taken to achieve the goal:

1. Analysis of deviations of areas virtually machined by the CAM system and analysis of deviations obtained by scanning actually produced surfaces.
2. Comparison of deviations and determination of the reliability of the CAM system in predicting the accuracy of milled surfaces.
3. Measuring and comparing the surface roughness of milled surfaces.

The sample with six hemispherical surfaces on cylindrical protrusions was designed - Fig. 1. The purpose of the protrusions is to allow good access of the tool and measuring devices to the assessed areas. The dimensions of the base are 100 x 67 mm, the radius of the hemispherical surfaces is 10 mm. The material of the sample is aluminium alloy EN AW 6061 T651. The workpiece has the same floor plan dimensions as the sample, its height is 26 mm.

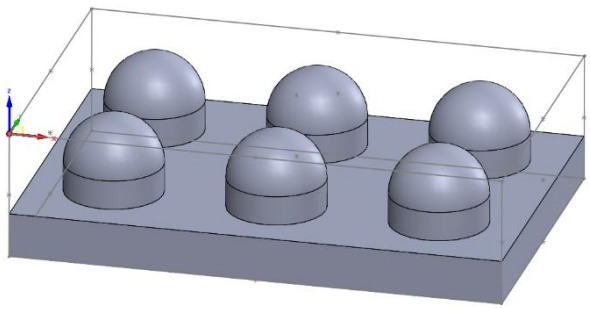

Fig. 1 *Sample with the outline of the workpiece*

Three frequently used strategies were selected, namely Constant Z, Radial, and Linear. The Linear strategy used the option of automatically generating additional paths rotated 90 ° to improve surface quality. The arrangement of the surfaces on the sample is shown in Fig. 2.

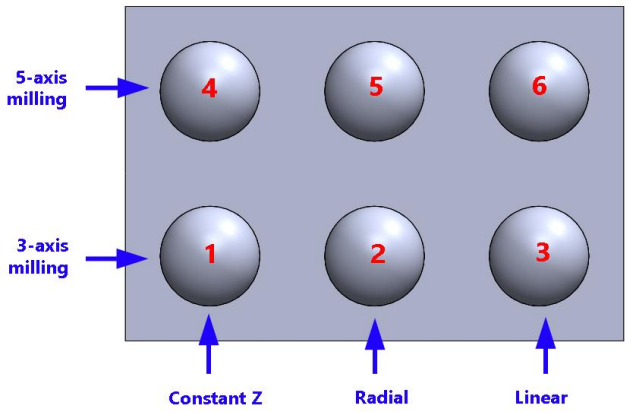

Fig. 2 *The arrangement of the surfaces on the sample*

The SolidCAM CAM system was chosen for the creation of NC programs. The advantage of the system is the ability to convert 3-axis milling operations to 5-axis while maintaining the main settings, which was fully utilized in the experiment. The postprocessor for a 5-axis continuous milling machine DMG Mori DMU 60 eVo was used to generate NC programs. The sample was made on this machine.

This machine is equipped with the Heidenhain TNC 640 control system. The generated NC programs were transmitted by the DNC network to the machine control system. The functionality of NC programs was checked in the simulation mode of the control system.

The roughing of the sample was carried out so that an addition of 0.25 mm remained on the hemispherical surfaces. The same parameters were used in the settings of all finishing strategies. The main requirement was the scallop height after machining, set at 0.005 mm and a tolerance of deviations of the shape of 0.01 mm.

The ball-end mill N.RD.10,0.45°.Z4.HA.K TI1000 with a diameter of 10 mm, manufactured by WNT with a set cutting speed v_c = 400 m.min^{-1} and a feed per tooth of 0.04 mm was chosen to finish the shaped surfaces. By converting 3-axis operations to 5-axis operations, the monitored settings were maintained. The position of the tool axis was controlled by a curve (circle) at a defined distance below the shape surface. The size of the circle and the distance control the inclination of the tool axis relative to the Z axis. The angle of the tool axis improves cutting conditions because a tool area with a low cutting speed is excluded from the cut.

3. Experimental works

A separate NC program was generated for each hemispherical surface of the sample. For the first three surfaces, made by 3-axis milling, the generation of orders was allowed only for three axes - X, Y and Z. For the other three areas, the generation of orders was also allowed for rotary movements A and B. The sample after the production of all shaped surfaces is shown in Fig. 3.

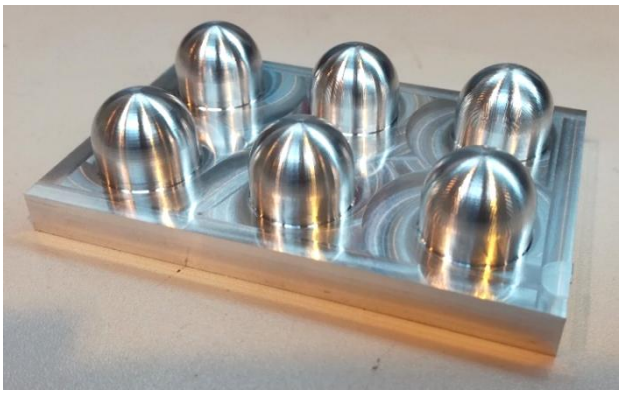

Fig. 3 *The sample after the production*

The HandySCAN BLACK Elite scanner was used to scan the samples, and the VXelements Viewer software was used to evaluate the scans. For comparison purposes, the color scale with the assigned deviation values was set identically in the CAM software and in the VXelements Viewer evaluation software - Fig. 4 and Fig. 5.

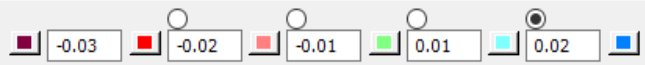

Fig. 4 *Color scale with assigned deviation values for CAM software*

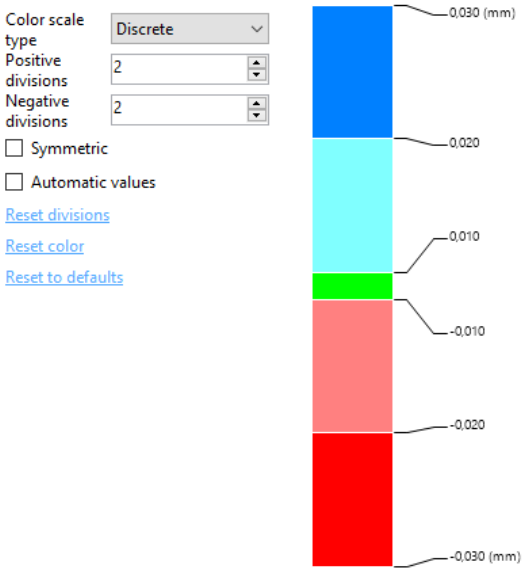

Fig. 5 *Color scale with assigned deviation values in the scanner evaluation software*

The result of the simulated CAM machining is shown in Fig. 6. The CAM system presented the virtual machined surfaces only with undercutting, the deviation in the positive direction (overcutting) was not presented. In 3-axis milling, undercutting exceeded -0.03 mm in all three strategies, the difference was in the distribution of undercut areas. The most significant undercutting is reflected in the Radial strategy in the form of several concentric circles.

In the 5-axis milling and Constant Z strategy, a surface without deviations was obtained. On the contrary, the Radial strategy undercut almost the entire hemispherical surface, with the undercut value exceeding -0.03 mm. With the Linear strategy, undercutting took place on about 50% of the area, the maximum value of undercutting also exceeded -0.03 mm.

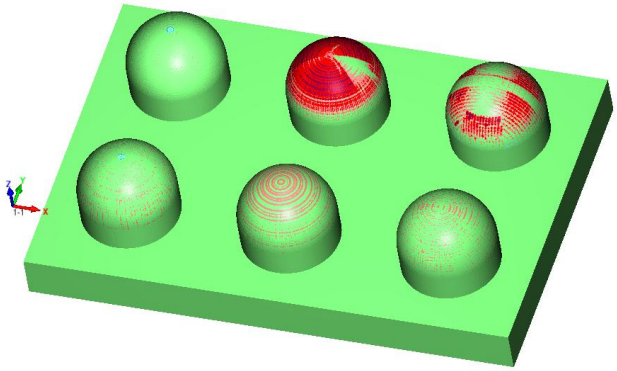

Fig. 6 *Deviations presented by the CAM system*

Scanning of the finished surfaces showed overcutting on all surfaces in the maximum value of 0.03 mm. The distribution of undercuts is similar in all cases – Fig. 7.

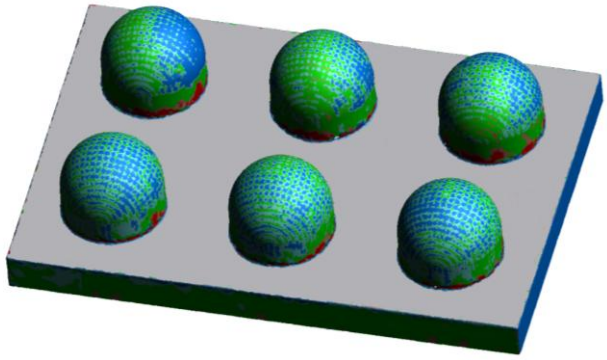

Fig 7 *Deviations obtained by scanning*

Mitutoyo Surftest SJ 410 was used to measure surface roughness. Four measurements were made on each surface – Fig. 8. The first two measurements were in the X-axis direction of the machine coordinate system on which the sample was made. The other two measurements were in the Y-axis direction. The instrument software recorded each measurement. The obtained profile is the result of filtering the measured profile by suppressing long-wave components, in this case in the shape of a semicircle. The results thus became relevant for roughness analysis. The cut-off value 0,8 mm was selected as recommended by standard ISO 4287: 1997. In Fig. 9 is an example of a roughness measurement record for one of the surfaces.

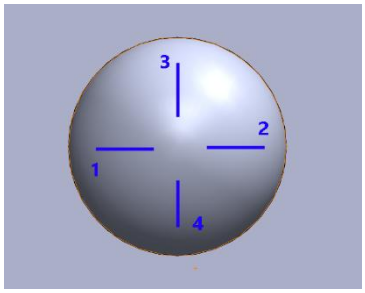

Fig. 8 *The order of measurements on each surface*

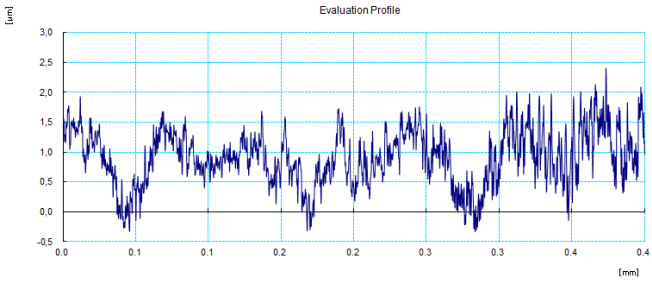

Fig. 9 *Surface roughness measurement record*

The values of the most common parameters Ra (arithmetical mean roughness value) and Rz (mean roughness depth) were recorded. The mean value was calculated from four measurements on each area. The values thus obtained are given in Tab. 1.

Table 1 *Mean values of parameters*

Milling method	Strategy	Ra [µm]	Rz [µm]
3-axis	Constant Z	1,05	4,33
	Radial	0,98	2,73
	Linear	1,26	5,54
5-axis	Constant Z	1,04	4,43
	Radial	0,94	2,44
	Linear	1,13	4,00

The comparison of the roughness of surfaces made by 3-axis and 5-axis milling through the parameter Ra is in Fig. 10, the comparison through parameter Rz is in Fig. 11. The Constant Z and

Radial strategies achieved very similar values. There are more significant differences in the Linear strategy, where the values are lower in 5-axis milling.

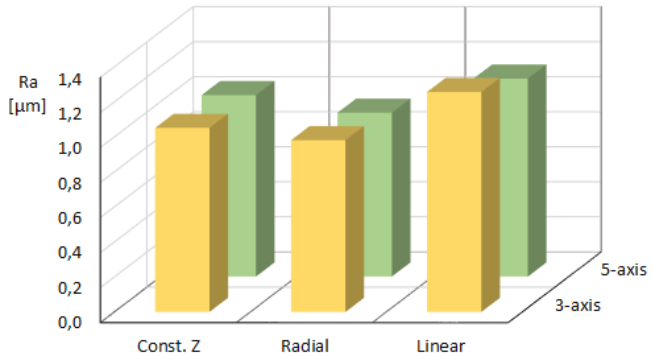

Fig. 10 *Comparison of the surface roughness parameter Ra*

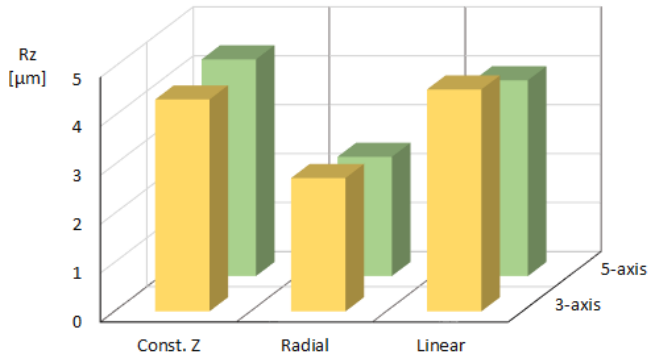

Fig. 11 *Comparison of the surface roughness parameter Rz*

4. Discussion

The prediction of residual material and undercutting in the CAM system did not correspond to the facts actually found. In all cases, the CAM system predicted only negative deviations (undercutting). On the contrary, positive deviations were found by scanning the produced surfaces. The prediction of milled surfaces by the CAM system is not convincing. However, such predictions are not unnecessary, they allow CNC programmers to better evaluate the milling process when selecting an effective toolpath strategy and milling method. The obtained results cannot be generalized, because each CAM system works with a different mathematical model and the results, especially in 5-axis milling, depend on the setting of a number of parameters.

Finishing operations take up approximately 70% of the total machining time for the production of shaped surfaces. Surface roughness is a key indicator of surface quality. Therefore, it is important to optimize the relationship between the milling parameters and the surface roughness of the finished part. This will eliminate or minimize finishing operations such as polishing or EDM.

The evaluation of the achieved surface roughness shows that with the Constant Z and Radial strategies, the milling method has a small effect on the surface quality. Linear strategy achieved better results with 5-axis milling compared to 3-axis milling.

Surface roughness depends on many factors. The parameters with the greatest influence are stepover and feed per tooth, the position of the tool in relation to the machined surface is also important. In general, 5-axis milling produces a more favourable surface quality, a smaller and more balanced value of the parameter Rz due to the constant position of the tool relative to the surface to be machined. This finding was only partially confirmed by the performed experiments.

It should be noted that the results obtained by similar experiments depend on many decisions and settings. The results can be influenced by the sample material, tool, strategies, machine, programming method, and the used programming system. The study provides a trend in the quality of treated surfaces under conditions similar to those used.

Acknowledgement: This research was funded by the Scientific Grant Agency of the Ministry of Education of the Slovak Republic (projects VEGA 1/0457/21 and KEGA 048TUKE-4/2020).

5. References

1. Bologa, O., Breaz, R.E., Racz, S.G., Crenganiș, M. Decision-making tool for moving from 3-axes to 5-axes CNC machine-tool. Procedia Computer Science 2016, 91, 184 – 192
2. Sadílek, M., Poruba, Z., Čepová, L., Šajgalík, M. Increasing the Accuracy of Free-Form Surface Multiaxis Milling. Materials 2021, 14, 15 p
3. Sadílek, M., Kousal, L., Náprstková, N., Szotkowski, T., Hajnyš, J. The Analysis of Accuracy of Machined Surfaces and Surfaces Roughness after 3axis and 5axis Milling. Manufacturing technology 2018, 18, 1015 – 1022.
4. Stejskal, M., Vavruška, P., Zeman, P., Lomička, J. Optimization of Tool Axis Orientations in Multi-Axis Toolpaths to Increase Surface Quality and Productivity. Procedia CIRP 2021, 101 69–72.
5. Batista, M.F., Rodrigues, A.R., Coelho, R.T. Modelling and characterisation of roughness of moulds produced by high-speed machining with ball-nose end mill. J. of Engineering Manufacture 2015, 1–12.
6. Shchurov, I.A, Al-Taie, L.H. Constant Scallop-Height Tool Path Generation for Ball-End Mill Cutters and Three-Axis CNC Milling Machines. Procedia Engineering 2017, 206, 1137–1141.
7. Kolar, P., Sulitka, M., Matyska, V., Fojtu, P. Optimization of five axis finish milling using a virtual machine tool. MM science j. 2019, 3534-3543.
8. Vakondios, D., Kyratsis, P., Yaldiz, S., Antoniadis, A. Influence of milling strategy on the surface roughness in ball end milling of the aluminum alloy Al7075-T6. Measurement 2012, 45, 1480–1488.
9. Bagci, E. Yüncüoğlu E.U. The Effects of Milling Strategies on Forces, Material Removal Rate, Tool Deflection, and Surface Errors for the Rough Machining of Complex Surfaces. J. of Mechanical Engineering 2017, 63, 643-656.
10. Shajari, S., Sadeghi, M.H., Hassanpour, H. The Influence of Tool Path Strategies on Cutting Force and Surface Texture during Ball End Milling of Low Curvature Convex Surfaces. The Scientific World J. 2014, 14 p.
11. Mali, R. Aiswaresh, R., Gupta, T. V. K. The influence of tool-path strategies and cutting parameters on cutting forces, tool wear and surface quality in finish milling of Aluminium 7075 curved surface. The Int. J. of Advanced Manufacturing Technology 2020, 108, 589–601.
12. Souza, A.F., Machado, A., Beckert, S.F., Diniz, A.D. Evaluating the roughness according to the tool path strategy when milling free form surfaces for mold application. Procedia CIRP 2014, 14, 188 – 193.
13. Ramos, A.M., Relvas, C., Simões, J.A. The influence of finishing milling strategies on texture, roughness and dimensional deviations on the machining of complex surfaces. J. of Materials Processing Technology 2003, 136, 209–216.
14. Logins, A., Torims, T. The Influence of High-Speed Milling Strategies on 3D Surface Roughness Parameters. Procedia Engineering 2015, 100, 1253 - 1261.
15. Sales, H.R., Amirabadi, H., Hosseinabadi, H.N., Bagheri, M.R. Experimental Study of Tool Path Strategies for Three and Five axes Milling along with Feed Rate Optimization. Indian J. of Science and Technology 2016, 9, 1-12.

Disposal of Spent Ionizing Radiation Sources Cobalt-60

Ulugbek Ashrapov*[1], Ilkham Sadikov[1], Bakhodir Mirzaev[1], Shavkat Malikov[1], Valery Nesterov[2]
Institute of Nuclear Physics of Academy Sciences (INP AS), Tashkent, Uzbekistan[1]
Joint Stock Company «National Technical Physics and Automation Research Institute», Moscow, Russia[2]
ashrapov@inp.uz

Abstract: *The paper discusses the experience of work of specialists of the consortium as part of the INP AS (Tashkent, Uzbekistan), JSC "National Technical Physics and Automation Research Institute" and CJSC "Mounting Firm "Radiy" (Moscow, Russia) at utilization of 96 pieces of sources GIK-7-2 Co-60 of gamma installations of "RKhM-gamma-20" and "Issledovatel", including 2 emergency sources Co-60, their burial in specialization point for radioactive waste. Also, the experience of specialists in the elimination of emergency situation with recharge a highly active source of GIK 8-4 Co-60 for radiation gamma therapy from emergency holder with crack to a new holder from depleted uranium. The reason for the appearance of a crack on the body of the Co-60 source holder is discussed.*
Keywords*: RADIONUCLIDE Co-60, EMERGANCY SITUATION, GAMMA-INSTALLATION, SOURCE HOLDER, DEPLATED URANIUM, RADIOACTIVE WASTE.*

1. Introduction

Radiation technologies in scientific research, irradiation of materials and foods, gamma therapy in oncology is based on use gamma-radiation of closed source of ionizing radiation with radionuclide Co-60, which has a half-life of 5.2714 years and very hard energy of gamma radiation (1.732 and 1.3325 MeV). Sealed sources GIK 8-4 and GIK 7-2 Co-60 belong to dangerous radioactive sources of category 1 [1] and if safety rules are not observed or their protection is not reliable, they can cause irreparable harm to human health and the consequences can be fatal.

There are 16 large medical institutions in Uzbekistan with devices for radiation gamma therapy with Co-60 sources for oncological dispensaries, as well as a gamma installation with GIK-7-4 sources at the INP AN in Tashkent and a gamma installation GUBE-6000 of the Veterinary Research Institute with GIK- 7-2 in Samarkand region. Currently, the actual tasks are the utilization of expired Co-60 sources, and the related training of personnel to work with Co-60 sources, the development of technologies, special instruments and equipment used for their disposal. To work with high-level sources of Co-60, a consortium was created consisting of specialists from JSC "NIITFA", CJSC "MF" Radiy "and the Institute of Nuclear Physics of the Academy of Sciences of the Republic of Uzbekistan, the purpose of which is to utilize sources of ionizing radiation Co-60 GIK 8-4 and GIK 7-2 and eliminate emergencies with them.

The article is aimed at presenting the experience of the consortium in the elimination of accidents with high-level sources of Co-60, as well as their disposal.

2. Materials and methods.

Gamma-installations «RKhM-γ-20» and «Issledovatel» of JSC «Foton» were designed to conduct radiation research in the field of solid state physics, radiobiology, medicine and production and technological processes for gamma irradiation of semiconductor products. The assigned life of Co-60 sources has expired six times, however, the total activity of 96 pcs. sources of Co-60 GIC 7-2 in both gamma installations was 2.056 ·1013 Bq (555.4 Ci).

To discharge Co-60 sources from gamma-ray plants, a reusable transport packaging kit UKT-1V-26-12 with a rechargeable container KTB-250-12 was used (Fig. 1).

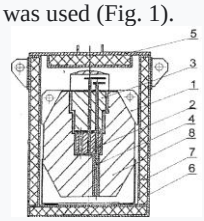

Fig. 1. *Scheme of the transport packaging kit UKT1V-26-12: 1 - KTB-250-12 rechargeable container; 5 - cover of the protective container; 2 - drum; 6 - body of protective packaging; 3 - cork; 7 - thermal protection.*

In Table 1 are shown specifications of the UKT1V-26-12 packaging kit.

Table 1. *Technical characteristics of the packaging kit UKT1V-26-12.*

Facing	Steel type X18H10T
Protection	Lead
Maximum container dimensions	diameter – 680 мм, height – 860 мм
Nest dimensions	diameter - 14 мм, height – 105 мм
Weight, kg	2320
Number of working channels	12
Permission loading sources Co-60	up to 25 kCi

Installations "RKhM-γ-20" and "Issledovatel" are lead containers, in the center of which there are working chambers located around the circumference with tubular cassettes ("squirrel wheel"), each of which could accommodate up to 6 GIK 7-2 sources Co-60 with dimensions: Ø=11.2 mm, h=81.5 mm. Fig. 2 shows the structural diagram of the "Issledovatel" gamma installation [2].

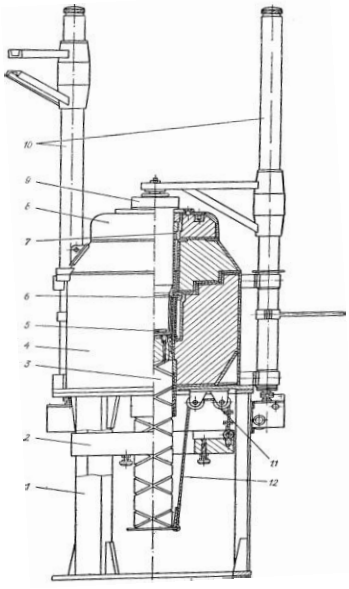

Fig. 2. *Structural scheme of the "Issledovatel" gamma-installation: 1 - bed; 2 - counterweight; 3 - stock; lead container (radiation head); 5 - work table; 6 - cylindrical irradiator; 7-beam shutter; 8-shutter body; 9-cork; 10-lift mechanism; 11 - blocks; 12-cables.*

For the removal of GIK 7-2 Co-60 sources from the «RKhM-γ-20» and «Issledovatel» gamma-installations, standard collets and

rod rigs were used. Fig. 3 shows a general view of the collets, rods and non-standard tools for removing 2 emergency Co-60 sources.

a b c

Fig. 3. *Photo view of the collet (a), rod (b) and developed a new non-standard tools (c) for the removing 2 emergency Co-60 sources.*

Non-standard tools are hollow tubes with pointed ends that attach to a drill and do the job of removing the epoxy around the Co-60 source.

The specialists with DPG-03 thermoluminescent dosimeters and «Rados-60» dosimeters were provided. Dosimetric control of the exposure dose rate with an IdentyFINDER R400 dosimetric device was carried out. The radiation-hazardous work of the personnel was carried out under constant dosimetric monitoring of the radiation level in compliance with sanitary standards and radiation safety requirements of SanPiN No. 0193-06 [3].

3. Results and discussion

The consortium performed work on the radiation-safe mode of unloading 96 sources of Co-60 GIK 7-2, including 2 emergency sources from the gamma-ray installation "Issledovatel", they were transported by special vehicles during 4 times (total 560 km) from JSC "Photon" (Tashkent city) to the Republican State Enterprise for the Disposal of Radioactive Waste (Tashkent region) accompanied by a police convoy and were buried in the storage of spent radioactive sources. An emergency situation is present when discharging from a gamma plant 2 emergency sources of Co-60, which are present in the hardened epoxy resin. In this emergency situation, standard equipment could not be used, so a non-standard tools was developed. Fig. 4 shows the use a non-standard tool for removing emergency sources 2 that were in the hardened epoxy resin and specially designed tools were used to destroy the epoxy resin (a).

a b c

Fig. 4. *Destruction of epoxy resin (a), removal of emergency Co-60 sources from the «Issledovatel» gamma-installation (b), dismantling of the KTB-250-12 recharge container with Co-60 sources (c).*

Another work of the consortium was the elimination of an accident with a 1 peace Co-60 source in an emergency holder of a gamma therapeutic remote apparatus of the Namangan Regional Oncological Dispensary, where the emergency situation arose due to a jamming in a transport and reloading container of the KTP-5M type of a clip with radioactive cobalt-60 of the GIK 8-4 type with an activity of 3750 Ci. The holder together with the source could not be removed from the rechargeable container using standard technology, which required the return of Co-60 to the manufacturer from the Russian Federation. Emergency situation by the personnel using special equipment with remote manipulators in a protective box was resolved. In the protective box, the holder with the Co-60 source was removed through the inlet channel using remote manipulators, the source was transferred to a new holder, which was then placed in the KTP-5M container in accordance with the flow chart (Fig 5).

a b

Fig. 5. *Preparatory work with recharge container KTP-5M (a) and recharging of the Co-60 source from the emergency holder into a new holder in protective box (b).*

The dosimetrically measurements on Radiagem-2000 radiometer and gamma spectrometric measurements immersion liquid on DSA-1000 digital multichannel spectrum analyzer with Genie-2000 software (Canberra, USA) were carried out.

The exposure dose rate (EDR) on the surface of the recharge container KTP-5M was 10.8 μSv/h, while the EDR in the working room was 0.25 μSv/h. After removing the Co-60 source from holder, a visual inspection of the holder body showed the presence of two longitudinal cracks on its serface, as a result of which the holder body swelled and increased by 0.94 mm in diameter, which led to a problem with its removal through the outlet channel of the container for recharging. Fig. 6 shows crack on the body of source holder.

Fig. 6. *Crack on the body of the source holder.*

However, a crack in the body of the holder did not lead to a violation of the tightness of the Co-60 source itself, the tightness of which was checked by the immersion method [4]. The spectrometric analysis data of immersion liquid was showed that the Co-60 source is sealed (activity of immersion liquid is ≤185 Bk) [5] and no radioactive contamination of the holder body was found.

Fig. 7 shows a depleted uranium container (a) containing a source of Co-60 for disposal and a depleted uranium plug fully wedged into the container body due to expansion (b).

a b

Fig. 7. *Depleted uranium container (a) containing a source of Co-60 and a plug of depleted uranium that was completely wedged into the body of the container during expansion (b).*

The emergency situation could be eliminated and the container lid opened only by repeatedly exposing the plug to alternating low temperature with liquid nitrogen (-196 ^{0}C) and high flame temperature with a gas burner (+500 ^{0}C).

When analyzing the cause of a crack in the depleted uranium holder body or jamming of the depleted uranium container cap, it was concluded that in the presence of oxygen, water vapor can be adsorbed on the walls of the holder with depleted uranium, which reacts violently with uranium with the release of hydrogen, which reacts with uranium to form pyroform uranium hydride [6]. The ongoing chemical reactions can be represented by the following equation:

$$7U + 6H_2O = 3UO_2 + 4UH_3 + Q \uparrow \text{(evaporation)} \quad (1)$$

As is known, the density of depleted uranium is 19 g/cm³, therefore, with the complete oxidation of uranium due to oxygen and moisture from the air, a twofold increase in the volume of the holder is possible. The cause of corrosion in the body of the holder is the thermodynamic instability of the metallic state of depleted uranium. It should be note that the IAEA classifies depleted uranium as category II nuclear material and defines the levels of physical protection during storage and transportation [7], which means that the handling of depleted uranium requires precautions.

4. Conclusions

In total 96 pieces of exhausted Co-60 sources from the «RhM-γ-20» and «Issledovatel» gamma-installations at the appointed time and in compliance with radiation safety were discharged and utilizated as radioactive waste [8]. Non-standard emergency with the removal of two emergency sources of Co-60 from the gamma installation successfully was completed. The IAEA news reported on the successful completion of the project [9].

The highly active source Co-60 GIK 8-4 from the emergency holder into a new holder of the gamma therapeutic installation was recharged. Replacement of the depleted uranium holder with a new one guarantees its further performance for 15 years.

The results of work with depleted uranium products showed that hydrolysis corrosion is observed in majority depleted uranium products used for radiation protection against gamma radiation (radiation head of gamma flaw detectors, transport packaging containers and protective containers for high radioactive closed radiation ionizing sources).

5. References

1. Code of Conduct on the Safety and Security of Radioactive Sources. Vein. IAEA. 24 (2004)
2. Gamma-installation "Issledovatel". Technical description and instructions of operation. Moscow. 30 (1969)
3. SanPiN No. 0193-06. *Radiation safety standards and basic sanitary rules for ensuring radiation safety*. Tashkent. 92 (2006)
4. Ergashev Kh.A., Makhkamov Sh.M. Ashrapov U.T. *Leak test method source of ionizing radiation.* Patent of the Republic Uzbekistan, № 4943 (1997)
5. International Standard ISO 9978-92. *Radionuclide ionizing radiation sealed sources. Leakage test methods.* Washington. USA. 11 (1992)
6. Karnozov A.A. *Issues of protection of fissile materials in nuclear charges*. Solving the plutonium problem. JSC "High-tech Research Institute of Inorganic Materials named after Academician A.A. Bochvar". Digest of articles. 92-97 (2000). http://elib.biblioatom.ru/text/vniinm-50_t4_2000/go,2.
7. Information Circular of the IAEA. *The Convention on the Physical Protection of Nuclear Material* (1980). https://www.iaea.org/sites/default/files/infcirc274r1.pdf
8. Ashrapov U.T., Doroshenko A.A., Nesterov V.P., Tashmetov M.Yu., Filatov K.V. *Questions nuclear science and technology* Moscow. **76**. 53-56 (2017)
9. IAEA. News of the scientific portal "Atomic Energy 2.0" https://www.atomic-energy.ru/news/2016/05/20/66073

Investigation of the interface of two-layer diamond plates for drilling tools

Viacheslav Prokhorov, Sergey Perfilov, Anrey Pozdnyakov

Technological Institute for Superhard and Novel Carbon Materials, Moscow, 108840 Russia
Moscow Institute of Physics and Technology (State University), Moscow, 141701 Russia

*E-mail: pvm@tisnum.ru

Abstract: *Two-layer diamond-hard alloy plate is the cutting element of the drill bit and consists of a layer of polycrystalline diamond compact (PDC) binded with the superhard alloy substrate (WC-Co). PDC tools are now actively used in the drilling of mineral resources for the search and production of hydrocarbons.*

Full-scale tests of PDC cutters in PDC bits have shown that their strength, wearability, and especially heat resistance, are determined by the quality of the contact layer (interface) between the PDC and the substrate. In the work, the interface of the diamond layer and the substrate of two-layer diamond plates made on the installation based on a multi-punch press GY850 *was investigated by laser-ultrasonic flaw detection.*

***KEYWORDS**:* SUPERHARD MATERIALS, POLYCRYSTALLINE DIAMOND COMPACT (PDC), PDC CUTTER, LASER-ULTRASONIC FLAW DETECTION, INTERFACE PROPERTIES

1. Introduction

Superhard materials [1] are widely used in processing tools, among them the most well-known are Polycrystalline Diamond Compact (PDC) and Polycrystalline cubic Boron Nitride (PcBN). PcBN tools are mainly used for the treatment of iron-based hard alloys, while PDC are more commonly used for the treatment of highly abrasive non-ferrous alloys and composites.

PDC tools are now actively used in the drilling of mineral resources for the search and production of hydrocarbons [2]. The basic tool of drilling equipment is the milling bit of rotary drilling (Fig. 1, a), the cutting elements (Fig. 1, b) of which move along the bottom of the well and cut the rock.

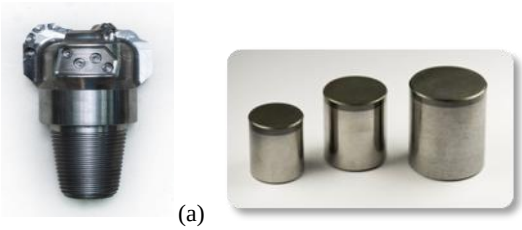

(a) (b)

Figure 1. The working part of the milling drill bit (a) and PDC cutters (b).

Although the cost of bits equipped with PDC-cutters is a few percent of the total cost of the well, the drilling speed, the number of flights and the maximum length of well penetration, which determine the economic indicators of well development, depend on the quality of the cutting arms of the bits and their wear resistance. The improvement of the cutting elements of drill bits and service mechanisms improve stabilization of motion and reduce the vibration of the drill bit to facilitate rapid and efficient drilling.

Development of two-layer diamond plates is one of the tasks of creating in Russia a modern competitive on the world market of domestic production of tools for the manufacturing industry, oil and gas production and construction.

2. PDC-cutters made in FSBI TISNCM

PDC drill bit is a modern high-performance drilling tool for rotary drilling. PDC bits are drilled faster by cutting and consume less energy than rock chisels. The body of the diamond drill bit is equipped with PDC cutters, which destroy the rock cutting action, which is most effective when drilling hard stone. PDC cutters are developed and manufactured using the latest technology for drilling water, oil and gas wells or geothermal wells. They are a multi-component system, which includes: a) the diamond grains themselves, b) the binding phases used in the sintering process of the cutting PDC-elements and c) the method of connecting the diamond elements with the tool body. All elements require high-quality performance. Cutting elements are subject to severe abrasive-erosion wear conditions, causing heating to a high temperature. Not only the wear resistance of the PDC composite is crucial for the functional quality of the tool, but its thermal stability, thermal conductivity, impact resistance, thermal fatigue, strength and fracture toughness are equally important [3]. These properties determine the suitability of the diamond composite tool for the mining industry.

PDC cutter consist of diamond crystal grains, fused together with the participation of a metal "catalyst", which is usually cobalt. It also binds the PDC plate to the tungsten carbide substrate. Without cobalt, much higher pressures and temperatures would have to be applied to form a PDC compact, which today can not be applied in the field of mass production. However, the presence of cobalt in PDC cutters creates a problem when they are heated by intense abrasive friction during bit operation. First, the cobalt expands much more than the diamond, and destroys the PDC. Secondly, when heated, cobalt graphitizes diamond [4].

In PDC cutters developed in FSBI TISNCM the plate of PDC, 2-3 mm thick and up to 18 mm in diameter, is bonded with a substrate of hard alloy, forming the working element of the drill bit. PDC consists of a diamond frame with grains of 20-10 microns impregnated with a binder metal. The ratio of the diamond fraction and the binder metal, as well as the size of the diamond grains vary, depending on the specifications.

Figure 2. Installations for the manufacture of PDC cutters based on the GY850 multi-punch press.

PDC cutters are manufactured by the method of high pressure and high temperature using an installation based on the GY850 multi-punch press (Fig.2). Up to 12 PDC cutters are synthesized/sintered in one working cycle in a high-pressure chamber. After sintering, the surfaces of the PDC plates are ground and polished to the required values.

Full-scale tests of PDC cutters in PDC bits have shown that their strength, wearability, and especially heat resistance, are determined by the quality of the contact layer (interface) between the PDC and the substrate [5].

The paper presents the results of the study of the mechanical characteristics of PDC cutters, as well as the microstructure, element and phase composition and defects of the contact layer of PDC.

3. Studies of the interface characteristics of PDC cutters

In the previous work [5], we conducted a detailed study of the profiled interface on two samples of PDC incisors by non-destructive acoustic microscopy (AM) and on plates 4 mm thick cut from the central part of the PDC incisors. The study of the interface of a two-layer PDC/WC-Co plate revealed the presence of defects in the PDC layer. These defects, as a rule, in the form of pores up to 50 μm in size, are visible both on the AM images of the whole interface and the slice, and on the images of profilometry. AM flaw detection interface of the whole PDC cutter will reject the PDC cutters before connecting them to the bit.

In this work, we have made an attempt to evaluate the quality of the element interface by the non-destructive method of laser-ultrasonic flaw detection [6,7]. To assess the quality of the element interface, a laser-ultrasonic flaw detector UDL-2M was used (Fig.3.).

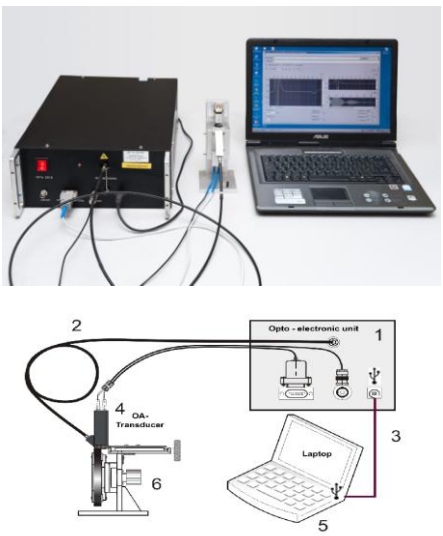

Figure 3. Laser-ultrasonic flaw detector UDL-2M.

The laser-ultrasonic flaw detector UDL-2M consists of the following main parts: 1 - optoelectronic unit, 2- fiber optic cable, 5 - information and measurement complex, 3- USB 2.0 connection cable, 4- OA generator.

The ultrasonic pulse generated by the laser is reflected from the interface of the diamond layer with the substrate (Pulse 1) and from the free boundary of the diamond layer (Pulse 2) (Fig.4.). The ratio of the amplitudes of these reflected signals can be used to judge the quality of the interface. In a sample with a good quality interface, the ultrasonic pulse passes completely through the interface and is reflected from the free boundary of the diamond layer of the PDC. Only the signal reflected from the free boundary is observed on the UDL-2M screen (Pulse 2).

Figure 4. Screenshot of the UDL-2M screen. Testing a sample PDC with a bad interface.

With the full passage of the ultrasonic signal through the boundary, the reflected signal (Pulse 1) is minimal, and the interface quality is good (Fig.5.).

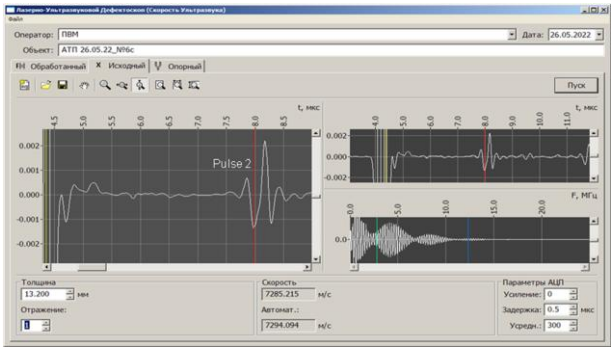

Figure 5. Screenshot of the UDL-2M screen. Testing a sample PDC with a good interface.

4. Conclusion

We tested 12 samples of the PDC cutters using the proposed non-destructive express method of laser-ultrasonic flaw detection. In the subsequent work, it is assumed that the data obtained will be compared with the results of mechanical tests of the quality of the interface of the PDC cutters.

5. Acknowledgments

The work was done using the Shared Research Facilities "Research of Nanostructured, Carbon and Superhard Materials" FSBI TISNCM.

6. Literature

[1] Wentorf R., R. Devries, F. Bundy. Sintered Superhard Materials. Science. 208, (1980), P. 873.

[2] Besson A., B. Berr, Dillard et al. Oil and Gas Review. (Shlumberge, 2002), P. 4.

[3] Sergeichev K., Uspekhi Prikladnoi Fiziki. Diamond CVD coatings of cutting tools (review). 3, (2015), P. 324.

[4] Zhan G., A. Patin, R. Pillai, et al., in Proc. IADC/SPE Drilling Conference, IADC. Global leadership. Global challenges. (2014, Castagna, FEI).

[5] Prokhorov V., Pozdnyakov A, Kravchuk K., Morokov E. Machines, Technologies, Materials. Issue 7, (2019), P. 294.

[6] Prokhorov V., G. Pivovarov. Ultrasonics. 51, (2011), P. 715.

[7] Prokhorov V., V. Blank, D. Ovsyannikov, M. Popov, V. Levin, E. Morokov. Machines, Technologies, Materials. Issue 22, (2015), P.44.

About corrosion damage of the railway wheels

Svetlana Gubenko
Iron and Steel Institute of National Academy of Science of Ukraine,
Prydniprovska State Academia of Civil Engineering and Architecture
Dnepr, Ukraine
sigubenko@gmail.com

Abstract.. *Corrosion mechanism and rate of different chemical composition and structural condition of wheel steel were investigated. It was shown that "white layers", variation in grain size and banding of wheel steel structure results in corrosion rate. Microstructure of steel from different elements of railway wheels after operation with corrosion was investigated. Wheel steel with addition of vanadium corroded more quickly than steel without vanadium. Non-metallic inclusions are the centres of corrosion nucleation and their influence on corrosion depends on type of inclusion. Mechanism of corrosion of wheel steel corrosion was discussed.*
KEYWORDS: *WHEEL STEEL, RAILWAY WHEELS, CORROSION DAMAGE*

1.Introduction.

Operation and transportation of railway wheels are realized without effective anticorrosion protection. The increase in the influence of aggressive environmental factors by large industrial enterprises exacerbates the problem of preventing the corrosion damage of railway wheels [1 - 7]. Railway wheels are exposed to corrosion during operation. Corrosion fracture of steel promotes embrittlement of wheels [8 - 10]. Corrosion of different parts of railway wheel takes place in dynamic and static conditions (atmospheric, wet, soil, gas, sea-water, stress, fretting, stray-current corrosion). The goal of this work is the compare investigation of corrosion rate of wheel steel with different structure from different elements of wheels after hot deformation, heat treatment and operation.

2. Materials and Procedures.

Microstructural research of wheel after operation was done. Structural changes near tread were researched in worn-out wheel 1. The zones of corrosion in different parts of wheel 1 and non-operated wheel 3 were studied. Selection of specimens for corrosion tests were realized from different parts of tread, rim and disk of wheels 1 and 2 after operation (5 years), non-operated wheels 3 and 4. Wheel 4 was produced from steel with microalloying of vanadium, wheels 1 – 3 were from usual wheel steel. Chemical composition of wheels are given in Table 1.

Table 1. *Chemical composition of wheel steels*

Wheel	Contents of elements, %								
	C	Mn	Si	S	P	Cr	Ni	Cu	V
1	0,59	0,72	0,34	0,025	0,012	0,14	0,15	0,20	-
2	0,65	0,79	0,36	0,027	0,010	0,13	0,18	0,18	-
3	0,61	0,78	0,30	0,029	0,024	0,17	0,15	0,16	-
4	0,46	1,04	0,47	0,024	0,018	0,09	0,11	0,18	0,10

Accelerate corrosion tests were carried out in special camera with moist atmosphere contained 10 mg/m^3 SO_2, also NO, NO_2 at temperature 20-25^{0}C, time 25 days. These conditions are coincided with industry atmosphere [11], but in another operation conditions atmosphere may be aggressive too by wet, soil, sea water, etc. Before corrosion tests specimens were weighed and all their faces were covered by paraffin but one of them was exposed to corrosion.

Microstructure of corrosion zones of wheel steel before and after operation of railway wheels and also after hot deformation and heat treatment was investigated with optical microscope "Neohpot-21" and scanning microscope JSM-35.

3. Results and discussion.

Examination of wheels 1 and 2 after operation was shown that many parts of their surface are covered by rust. Oxidation of steel takes place on tread, disk, hub. The particles of oxides were discovered by metallographic research (Fig. 1). Oxidation of steel is started from surface and penetrated to considerable depth. Thus long operation of railway wheels allow to show big sections of the corrosion.

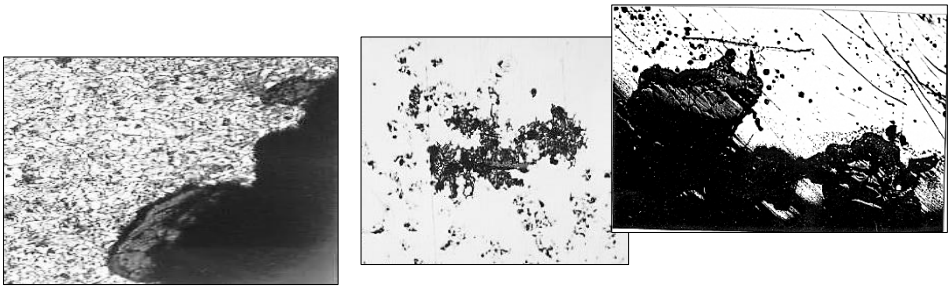

a b c

Fig. 1. *Sections of corrosion in railway wheels 1 and 2: a, c –x500, b –x200*

It is interesting to research role of corrosion processes in the development of structural changes near tread during operation of railway wheels. Macrostructural analyses of wheel 1 with heavy worn-out tread was discovered fatigue-corrosion wear accompaned distorting of the tread profile. Lots of the cracks with corrosion of steel were shown from the slidder to depth parts of the wheel. Microstructure of wheel rim near tread is characterized by presence of deformed grains zone and also sections of "white layer" [12 - 15]. The nature of structural changes is due to the combined action of thermal, dynamic and contact stresses arising in the interaction zone of wheel-rail rolling surfaces [16 - 19]. The important role of the structure of the outer surface of the wheels, which takes on external influences, should be taken into account [20 - 22].

Analyses of metallography investigation results allows to assept that structural changes happened near tread of railway wheel are accompaned by corrosion (Fig. 2). Zones of corrosion fracture were discovered along section of rim in areas with strong deformed structure also in areas of "white layer". By the roll formation on the side of rim when thin layers of steel are removaled to side of rim and disposed one over another the areas with oxidated surface of steel are finded oneself in internal parts of rim. They are arrenged between layers of deformed metal. Evidently presence of large oxide particles promotes not only to local fracture of tread areas but also to heterogeneous development of structural changes in thin layer of metal.

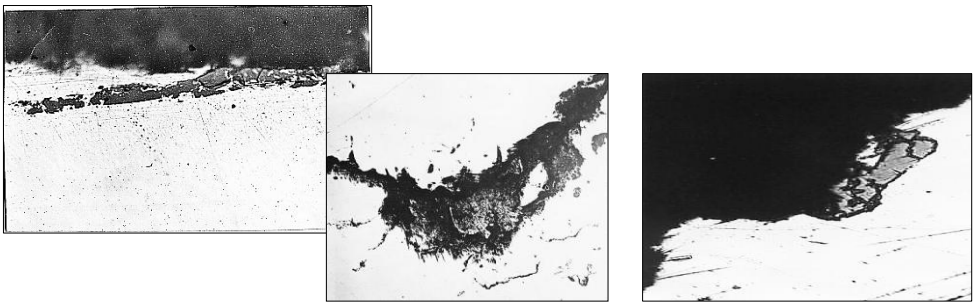

a b c

Fig. 2. *Sections of corrosion near tread of railway wheel 1 and 2 after operation: x500.*

Structural changes happened near tread were promoted different behavior of wheel steel by corrosion tests. Specimens from shabby wheels 1 and 2 were exposed to corrosion tests. Specimens from wheels 1 corroded with different rate which was decreased from cove zone along rim width and only near end of tread in the roll zone it again was increased (Fig. 3, curve 1). Thin parts of "white layer" corroded very quickly and were not discovered in structure of steel.

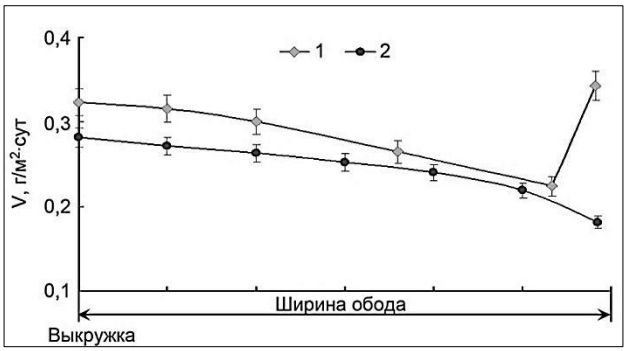

Fig. 3. *Change of corrosion rate V of specimens of wheel steel from tread along width of wheels 1 and 2 rims*

Change of corrosion rate and mechanism is obviously connected with change of character of plastic shear zone. In cove zone where grains are elongated and thin layer of steel was strongly deformed corrosion rate was maximum. Numerous small (< 20 mcm) oval pockets of localized corrosion were discovered, which were penetrated to considerable depth. In the time of corrosion the layer of elongated grains almost fully dissapeared. Maximum corrosion rate in the cove zone are explained by influence of plastic deformation created stresses in metal. In the middle of tread character of corrosion was changed. Along surface of specimens porosity corrosion film was formed and microcracks near oxides were discovered. Corrosion rate of specimens from the middle of tread and along to side of rim is essentially lower. In roll zone corrosion rate was increased again (Fig. 3, curve 1), and large pockets of the pitting corrosion were discovered. Their average size was 0,6 mm. Increase of corrosion rate of wheel steel in roll zone is explained by influence of considerable plastic deformation and also by the presence of cracks between layers of the rollig metal. Pockets of corrosion in roll zone are considerably larger then in cove zone. Thus heterogeneous plastic deformation along tread tooking place during operation of railway wheels promotes to heterogeneous corrosion fracture of tread.

Specimens from shabby wheel 2 also were corroded with different rate which was decreased from cove zone along width of rim (Fig. 3, curve 2). "White layer" was pittineged by the pitting corrosion practically on the all depth. In areas with base structure of steel (pearlite + ferrite) and small zones of "white layer" corrosion was founded on surface and penetrated deep into steel by cracks or by compact front. From the corrosion areas microcracks were penetrated into interphase boundaries ferrite-pearlite and also by

pearlite, which has well-developed interphase boundaries ferrite-cementite.

Corrosion of specimens from central part of rims of wheels 1 and 2 took place by formation of large pockets of oxidation of steel. Pockets of corrosion were formed on the surface of specimens and then were penetrated into depth of specimens and were grown by width to the contact one another. Under corrosion in oxides and on the interphase boundaries oxide-steel structural and phase stresses and microcracks were founded. Sizes of pockets of corrosion in these cases are 1…2 mm. Corrosion rate of rim metal of wheels 1 and 2 possessed ferrite-pearlite structure are approximately the same and was higher than corrosion rate of steel from tread (Tabl. 2).

Metal of disk corroded more quickly than metal of central part of rim (Tabl. 2). Corrosion process was spreaded along pearlite areas, and also along ferrite-pearlite boundaries. Kind of corrosion damages of metal from rim and disk is different: in the first case small pockets of corrosion were discovered, in second case large pockets of corrosion were discovered. From the pockets of corrosion intercrystalline cracks were spreaded along pearlite and ferrite-pearlite boundaries. Corrosion rate of specimens from disk of wheel 1 was a little higher then corrosion rate of disk of wheel 2.

Table 2. *Results of corrosion tests of wheel steels*

Wheel №	Place of specimens selection	Microstructure of wheel steel	Corrosion index		h, mcm
			K_1,g/cm^2	K_2,g/m^2.h	
1	middle of tread after operation	elongated grains of ferrite and pearlite	24,058	0,408	222
2		“white layer”	22,9643	0,359	204
1	central part of rim after operation	equiaxed grains of ferrite and pearlite	13,30	0,225	140
2		equiaxed grains of ferrite and pearlite	17,0642	0,289	125
1	disk after operation	ferrite and pearlite, banding	21,7702	0,389	166
2		ferrite and pearlite, no banding	22,8889	0,368	159
4	tread after heat treatment	sorbite of tempering	17,8182	0,302	148
4	central part of rim after heat treatment	ferrite and pearlite	18,8102	0,319	167
3	tread after heat treatment	sorbite of tempering	19,6316	0,327	115
3	central part of rim after heat treatment	ferrite and pearlite	24,069	0,401	138

Corrosion of specimens from tread of heat treated wheels 3 and 4 (with addition of vanadium) having structure of sorbite of tempering had lamellar or film character. Specimens from central part of rim of wheels 3 and 4 had the same character of corrosion (Fig. 4, a, b). Brittle cracks were spreaded from the porosity oxides to steel. Steel with addition of vanadium corroded more quickly than ordinary wheel steel (Tabl. 2). It is known vanadium promotes to decrease of corrosion resistance of steel and influence of manganese is the same [1]. The tread after heat treatment corroded more quickly than tread after operation. Corrosion of specimens from central part of rims of wheels 3 and 4 had pitting character with small pockets of corrosion and cracks were spreaded by the pearlite. Steel with addition of vanadium corroded more quickly than ordinary wheel steel (Tabl. 2). It is known the steels with martensite structure have a low corrosion resistance [1]. By heat treatment in martensite structure considerable stresses are formed which decrease corrosion resistance of steels. Also the martensite structure decreases the resistance of brittle fracture of steels. So martensite structure is inadmissible in railway wheels.

Investigation of corrosion product of wheel steel was discovered the heterogeneous structure of powder. Upper part is white powder – hydrate $Fe(OH)_2$, under it - red rust containing Fe_{com} - 48,25%, Mn - 0,37%, C - 2,87% (Fig. 5).

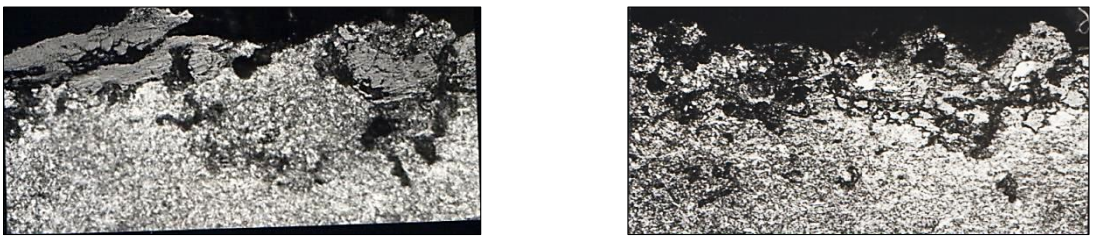

a b

Fig. 4. *Microstructure of surface of wheel steel specimens with addition of vanadium (a) and ordinary wheel steel (b) after corrosion tests: x200*

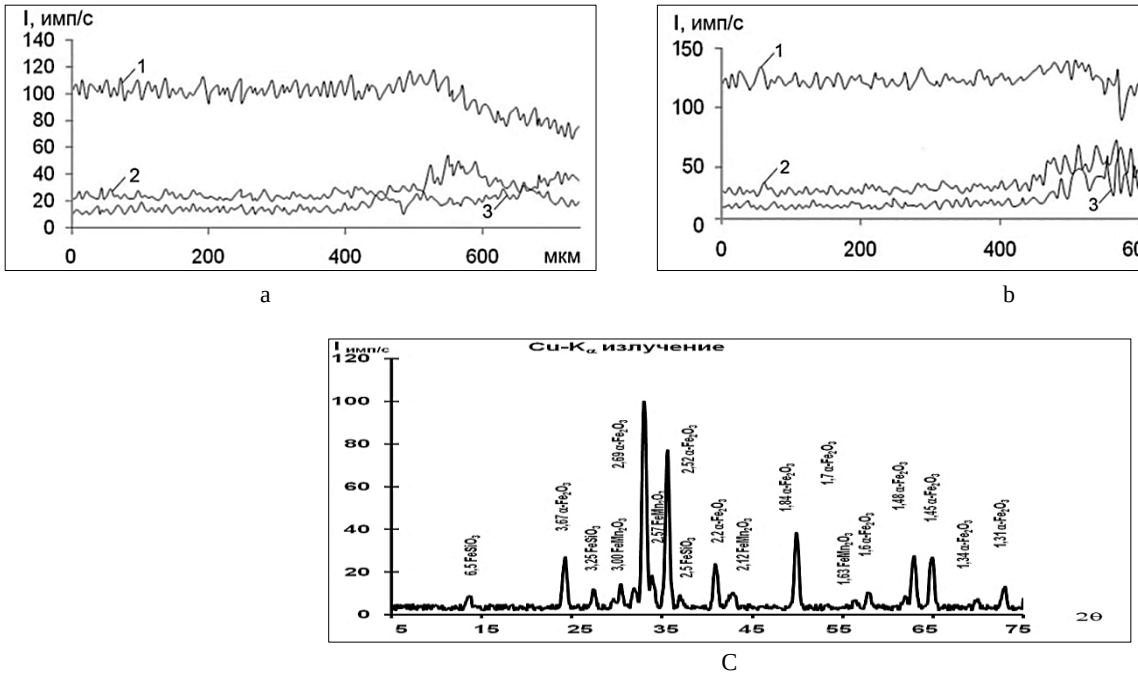

Fig. 5. *Distribution of chemical elements in oxide phases of corrosive origin (a, b; cur. 1 - Fe, cur. 2 - Si, cu. 3 - Mn) and the phase composition of corrosion products of the wheel steel (c)*

Different corrosion rate of wheel steel is explained by its different structural state. In worn-out railway wheels tread corroded more quickly than metal from central part of rim. This is explained by influence of stresses creating plastic deformation in thin surface layer. Areas of "white layer" on the tread promote delay of corrosion. These connect with ultrafine structure of the "white layer" [2, 3]. Metal from disk corroded more quickly than metal from central part of rim thanks to more rough of ferrite-pearlite structure of disk and also more ferrite banding of steel structure.

In heat treated railway wheels tread corroded more slowly than metal from central part of rim. This connect with more disperse ferrite-pearlite steel structure of tread after heat treatment. Microaddition of the vanadium promotes accelerate of corrosion of tread and metal from central part of rim.

Principles of wheel steel structure influence on the corrosion rate are confirmed also by results of definition of the depth of corrosion penetration *h* from surface to specimens having different microstructure (Tabl. 2). Average value of *h* was determined from the depth of all researching corrosion zones by metallography method. By analysis of these results it is necessary to take into value of *h* are cited for middle part of tread after operation

It is known the considerable thermal and deformational stresses causing by different physical-mechanical properties of non-metallic inclusions and steel matrix are exited near these particles [23]. Stresses are formed on the different stages of railway wheels production. Concentration of stresses promotes reinforcement of corrosion damage for all kinds of non-metallic inclusions. of wheels 1 and 2. But in cove zone of wheel 1 value of *h* was 342 mcm, in roll zone – about 600 mcm.

Thus corrosion rate is smaller when structure of the wheel steel is more disperse. Coarse-graininess, variation in grain size and banding of wheel steel structure promotes increase of corrosion rate.

Research of corrosion areas in railway wheels after operation and heat treatment before operation was shown the big influence of non-metallic inclusions on process of corrosion (Fig. 6). One of the main factors defining corrosion behavior of wheel steel is electro-chemical heterogeneity of railway wheel surface. Presence of non-metallic inclusions differing from steel matrix by physical-chemical properties results in corrosion microcells and reinforcement of electro-chemical heterogeneity of railway wheel surface [8, 9, 20, 23]. In wheel steel oxides Al_2O_3, $MnO{\cdot}Al_2O_3$, (Fe,Mn)O, sulphides (Fe,Mn)S, silicates SiO_2, $MnO{\cdot}SiO_2$, $FeO{\cdot}SiO_2$ and carbo-nitrides TiCN are present. All these non-metallic inclusions are cathodes by relation to metal matrix and they are arranged in order to decrease of the value of electrode potential difference of wheel steel surface near non-metallic inclusions in decreasing series: sulphides, corundum, silica, nitride of titanium. Increasing series by electrical resistance of non-metallic inclusions is the same.

Especially it is displayed by applying of the stresses. In our research the nucleation and localization of corrosion fracture of wheel steel was observed near different kinds of non-metallic inclusions in worn-out railway wheels and also in heat treated railway wheels.

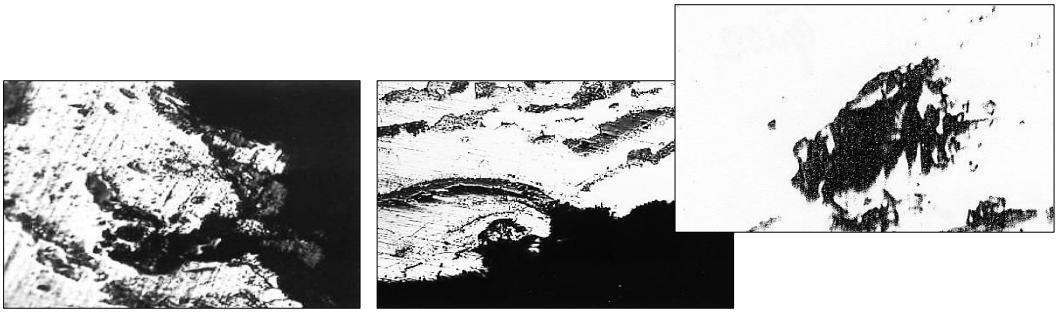

a b c

Fig. 6. *Corrosion fracture of wheel steel near non-metallic inclusions; x600*

Thus metallurgical factor namely contaminant of wheel steel by non-metallic inclusions is very important in the problem of corrosion fracture of railway wheels.

Corrosion is very dangerous for reliability and service life of railway wheels. It is known by the tests in air the time for nucleation of fatigue crack on the surface of metal can to compose till 90% from common service life of metal but corrosion promotes shortening of its share till 10% [5]. Chemical energy releasing in results of corrosion can to compose effective surface energy necessary for nucleation of crack. Wear-resistance of tread depends on surface condition. Formation of the oxides on the tread by corrosion of steel changes properties of this surface (strength, plasticity, wear-resistance) and influence on the condition of interaction between railway wheel and rail during operation.

4. Conclusions.

Corrosion of railway wheels during operation is decreased their reliability and service life. Mechanism and corrosion rate depend on chemical composition and structural condition of wheel steel. Non-metallic inclusions render great influence on corrosion fracture of railway wheels. It is necessary to work out anticorrosion actions during all stages of wheel production, keeping of railway wheels, their transportation to consumer and also their operation.

5. Literature.

1. Feraud P., Viet J., Diener M., Grab M.. Influence of corrosion on the behavior of wheelsets in service // The 15-th International Wheelset Congress (October 2007): Praga.Chesh. Repub, 2007, pp. 308-314.
2.. Beretta S., Carboni M., LoConte A.. Impact of corrosion upon fatigue properties of ainsteel // The 15-th International Wheelset Congress (October 2007): Praga.Chesh. Repub, 2007, pp. 294-300.
3. Resource and maintainability of wheelsets of rolling stock of railways / Vorobyov A.A., Gubenko S.I., Ivanov I.A. and others // Moscow: INFRA-M, 2011. – 264 p.
4. Influence of the structure and mechanical characteristics of wheel steels on the wear and modes of restoration of the profile of wheel sets /V.S. Kushner, A.A. Kutko, A.A. Vorobyov, S.I. Gubenko, I.A. Ivanov. // Omsk: ed. OmGTU, 2015. - 221 p.
5. Bogdanov A.F., Gubenko S.I., Zhukov D.A., Ivanov I.A. Surface layer and operational properties of the solid-rolled wheel rim \\ Structural and technological support of the reliability of the wheels of rail vehicles. Sat scientific. tr. PGUPS, St. Petersburg, 2009, pp. 15-23.
6. Changes in the rim surface and wheel life during operation / Bogdanov A.F., Budyukin A.M., Gubenko S.I., Ivanov I.A., Urushev S.V. // Structural and technological support of the reliability of the wheels of rail vehicles. Sat scientific. tr. PGUPS, St. Petersburg, 2009, pp. 23-40.
7. Bogdanov A.F., Gubenko S.I., Zhukov D.A., Ivanov I.A.. Surface Layer and Performance Properties of Solid Wheel Rim // Transport and engineering. Railway Transport, Scientific Proceedings of Riga Technical University, 2008, N 30, pp. 56-61.
8. Gubenko S.I., Pinchuk S.I., Belaya E.V.. Investigation of non-metallic inclusion effect on corrosion behavior of wheel steel. Metallurgical and Mining Industry, 2011, N 3 (2), pp. 63-66.
9. Gubenko S. I.. Influence of Nonmetallic Inclusions and Corrosion Products on the Wear Resistance of Railroad Wheels. Steel in Translation, 2019, v. 49, N. 6, p. 427–431.
10. Pinchuk S., Gubenko S., Belaya E.. Correlation between electrochemical corrosion and structural state of steel by simulation of operation conditions of railway wheels. Chemistry & Chemical Technology. Publishing House of Lviv Polytechnic National University, 2010, № 4 (2), p[. 151-158.
11. Karpenko G.V. , Vasilenko II. Corrosion cracking of steels. K .: Technique, 1971. - 191 p.
12. Taran Yu. N., Esaulov V. P., Gubenko S. I. Increase of wear-resistanceof railway wheels with different profile of trea. Metallurgical and Minning Industry, 2000, N 2, pp. 42-44.
13. Taran Yu. N., Esaulov V. P., Gubenko S. I. Structural changes in rims of railway wheels with different profile of tread. News of Higher Education. Black Metallurgy, 2989, N 9, pp. 101-105
14. Gubenko S., Proidak Y .. Investigation of wear mechanism of tread during operation of railway wheels. Transport problems, 2012, N 7, pp. 119-125.
15. Wear reduction on working surface of railway wheels / Taran Y, Yessaulov V, Sladkovsky A, Kozlovsky A, Gubenko S. WIT Transactions on Modelling and Simulation, 1970, v. 23, N 1, pp. 45-52.
16. Savrukhin A.V., Neklyudov A.N., Efimov R.A. Modeling of the thermal loading of solid-rolled wheels. World of Transport, 2014, N 5, pp. 22-30.
17. Stresses-deformed state of railway wheels of different design / Taran Uy., Esaulov V., Gubenko S., Sladkovsky A., Staroseletsky M. // Proceedings of the 13-th International Wheelset Congress (17-21 Sept. 2001). Rome: Italy, 2001, pp. 305-311.
18. An Analysis of Stress and Strain in Freight Car Wheels. / Sladkovsky A., Yessaulov V., Shmurygin N., Taran Y., Gubenko S. Transactions on Modelling and Simulation, 1997, N 16, pp. 15-24.
19. Rail vehicle dynamics and associated problems: monograph / Sladkowski A., Gubenko S., Pogorelov D., Iwnicki S., Licciardello R.V. Gliwice: Silesian University of Technology, 2005, 187 ppp.
20. Improving the performance of wheel sets of rolling stock / Valinsky O.S., Vorobyov A.A., Gubenko S.I., Ivanov I.A., Kerentsev D.E. Krotov SV , Urushev S.V. // Kazan, Izd.OOO "Buk", 2022. - 324 p.
21. Ivanov I.A., Gubenko S.I., Kononov D.P. Surface of machine and mechanism parts. St. Petersburg: LAN, 2021. - 156 p.
22. Gubenko Svetlana. Physical nature of the plasticity and strengthening of metals under deformation. Germany-Mauritius, Beau Bassin,: LAP LAMBERT Academic publishing, 2020. - 341 p.
23. Gubenko S.I., Oshkadepov S.P. Non-metallic inclusions in steel. – Kiev: Naukova dumka, 2016. - 528 p.

Analytical approach to crack tip plasticity of dental CoCrMo alloy

Martina Lovrenić-Jugović[1,*], Ljerka Slokar Benić[1] , Ivan Jandrlić[1]
University of Zagreb, Faculty of Metallurgy, Croatia[1]
mlovrenic@simet.unizg.hr

Abstract: *In this paper, a thin infinite plate of CoCrMo alloy with a straight crack was loaded perpendicularly to the crack plane. CoCrMo alloys are due to their suitable mechanical and corrosion properties widely used for dental applications. The importance of good mechanical properties is reflected in ensuring the functional and technical durability of dental appliances. The intention of this paper is to use a mathematical approach in analyzing a thin infinite plate with a straight crack to the rather complex occurrences within the cohesive zones around the crack tips. The dependence of plastic zone magnitude around the crack tip on an external load of dental CoCrMo alloy plate was considered in this paper. Static tensile tests were carried out to determine the mechanical properties of dental CoCrMo alloy. At plastic deformation, the dental CoCrMo alloy is nonlinearly hardened in accordance with the Ramberg-Osgood equation which parameters were determined using a least-squares method from experimental data. The application of the Dugdale model the plastic zone magnitude around the crack tip was determined. The stress intensity coefficient from the cohesive stresses was calculated using Green functions. The analytical methods, assuming a small plastic zone around a crack tip, were used in the analysis. The results were obtained by means of a commercial software package and presented in the form of diagrams.*

Keywords*: CrCoMo ALLOY, STRAIN HARDENING EXPONENT, DUGDALE MODEL, PLASTIC ZONE MAGNITUDE AROUND CRACK TIP*

1. Introduction

In spite of the fact that numerical methods are widely used in solving engineering problems in different fields of mechanics, in particular the finite element method, the analytical methods will be applied in solving the problems presented in this paper. A straight crack, with the length 2*a*, in a thin infinite plate loaded on its edges, is considered here. The plate is made of a ductile material (dental CoCrMo alloy); therefore, cohesive zones around crack tips occur when the plate is loaded. Our aim is to investigate the dependence of the magnitude of the plastic zone around crack tip r_p on an external load of dental CoCrMo alloy plate. The mechanical properties of dental CoCrMo alloy were determined by performing a static tensile test. It is an alloy that, in addition to the absence of nickel, its biocompatibility and corrosion resistance, has excellent mechanical properties such as hardness, tensile strength**,** and toughness [1]**.**

Since there is a lack of literature data investigating the dependence of the magnitude of the plastic zone around crack tip r_p of dental CoCrMo alloy, this paper deals with the analytical solution to the posed problem.

A thin, infinite plate with an embedded central straight crack of a length 2*a* was modelled analytically in this paper. A plate is uniaxially loaded in a direction perpendicular to the crack plane by monotonously increasing loading $\sigma_{yy}^{\infty} = \sigma_{\infty}$. A crack surface is unloaded. A plate material has the property of isotropic strain hardening (nonlinear strain hardening). A plane stress state is determined by the stress tensor components $\sigma_{xx}(x,y)$, $\sigma_{yy}(x,y)$ and $\sigma_{xy}(x,y)$ is assumed. For an analysis of the elastic-plastic fracture mechanics parameters, it is important to consider the stress tensor components and the displacement vector components of the points lying on a direction of a crack plane, i.e. on the *x*-axis. Since there is symmetry with respect to the *x*-axis, the shear stresses at the points laying on the *x*-axis will be equal to zero, i.e. the normal stresses $\sigma_{xx}(x,0)$ and $\sigma_{yy}(x,0)$ are the principal stresses. Equivalent stress σ_{equ} is determined according to the Tresca or the Mises yield criteria. The equivalent stress is dependent on the equivalent plastic strain $\varepsilon_{equ,p}$. Because a distribution law of equivalent plastic strain $\varepsilon_{equ,p}$ is not known, the distribution law of the cohesive stresses within a yield zone will be also unknown.

There are a great number of different methods, especially numerical, which can be used for determining the magnitude of the plastic zone around the crack tip. The Dugdale strip yield model [2-4] in the yielding zone around the crack tip is used for that purpose here. According to this model, the plastic zone is a narrow strip extending from the crack tip in the direction of the crack plane, as it is shown in Figures 1a and 1b. The Dugdale model considers, instead of a real, physical crack, an equivalent elastic crack of length 2*b*, as it is shown in Figure 1c. Partial areas of this imaginary elastic crack $a \le x \le b$ are subjected to nonlinear cohesive stresses $p(x)$, (Figure 1c).

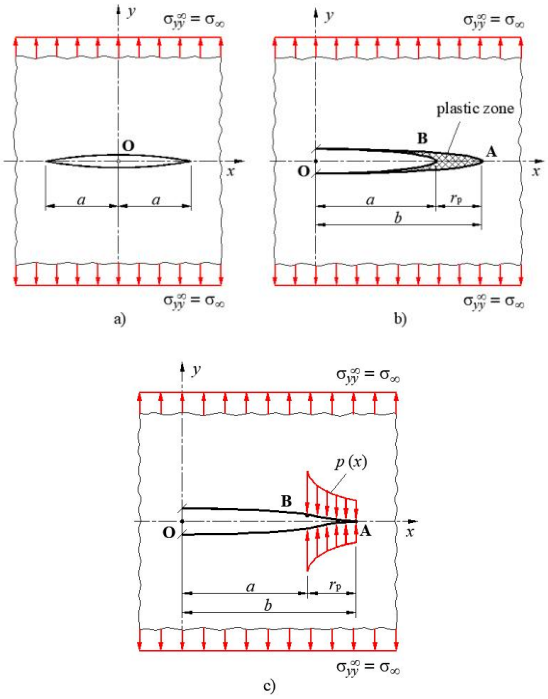

Fig. 1 *a) Thin, infinite plate with the straight crack of a length 2a loaded perpendicular to the crack plane,*
b) fictitious elastic crack including a small plastic zone around crack tip,
c) variable cohesive stresses act on a part of the fictitious elastic crack.

On the edges of plastic zones, or on the tips of an equivalent elastic crack, the normal stress $\sigma_{yy}(b,0)$ will not have singularity but will have a definite quantity equal to the yield stress of the plate material σ_0. In other words, the stress intensity coefficient *K* in these points will be equal to zero, i.e.

$$K(a+r_p) = K_{ext}(a+r_p) + K_{coh}(a+r_p) = 0 \qquad (1)$$

where K_{ext} and K_{coh} are the stress intensity coefficient of external and cohesive loading of the plate, respectively. The singularity at the tip of the fictitious elastic crack $x = b = a + r_p$, from the external load of the plate, is canceled with the singularity of the cohesive stresses within the plastic zone.

2. Mechanical properties of dental CoCrMo alloy

A static tensile test was performed to determine the mechanical properties of the dental CoCrMo alloy of the following chemical composition: 58.9–69.5% Co, 27.0–30% Cr, 5.0–7.0% Mo, with small quantities of Mn, Si, Ni, Fe, <0.05 wt.% C.

Two specimens according to DIN 50 125 - A6×30 shown in Fig. 2 were prepared for the static tensile test.

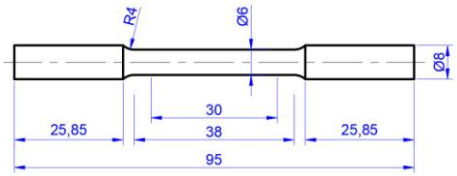

Fig. 2 *Dimensions of the specimen according to DIN 50 125 – A6×30*

Static tensile test was performed on a mechanical test machine Inspekt table 100kN according to DIN EN ISO 6892-1A, which includes the use of an external extensometer (see Fig. 3).

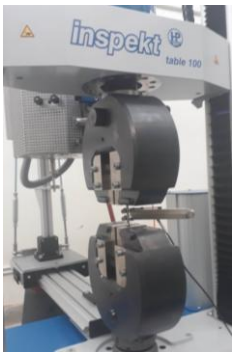

Fig. 3 *Static tensile test conducted with extensometer*

After the static tensile test, the engineering stress-strain dependences (Fig. 4) were obtained and shown in Table 1.

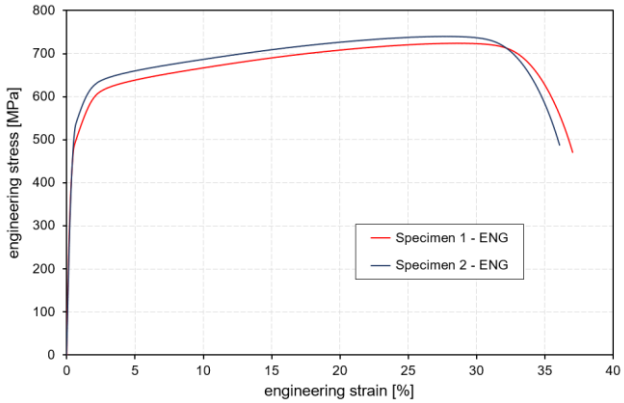

Fig. 4 *Engineering stress-strain diagrams of dental CoCrMo alloy*

Table 1: *Mechanical properties of dental CoCrMo alloy*

Specimen	Modulus of elasticity E [GPa]	0.2% offset yield stress $R_{p0.2}$ [MPa]	Ultimate tensile stress R_m [MPa]	Elongation A [%]
1	127.93	485.48	723.99	37.04
2	119.90	529.08	739.92	36.08

During the plastic deformation, the dental CoCrMo alloy is nonlinearly hardened and the correlation between stress and strain could be found in accordance with the Ramberg-Osgood equation, [5]

$$\frac{\varepsilon}{\varepsilon_0}=\frac{\sigma}{\sigma_0}+\alpha\left(\frac{\sigma}{\sigma_0}\right)^n \tag{2}$$

where σ_0 and ε_0 denote the material's yield stress and strain, respectively, while α and n denote Ramberg-Osgood's material constant and strain hardening parameter, respectively. If it is taken, the Ramberg-Osgood equation takes the form

$$\varepsilon=\frac{\sigma}{E}+\alpha\frac{\sigma_0}{E}\left(\frac{\sigma}{\sigma_0}\right)^n \tag{3}$$

According to Table 1, the dental CoCrMo alloy has a yield stress of 0.2% offset ($R_{p0.2}$). Instead of the yield stress σ_0 in equation (5), the 0.2% offset yield stress $R_{p0.2}$ was introduced. The plastic component of the strain tensor ε_{pl} has an amount of 0.002 for $\sigma=\sigma_0=R_{p0.2}$. Then equation (3) becomes

$$\varepsilon(\sigma=\sigma_0=R_{p0.2})=\frac{\sigma}{E}+\alpha\frac{\sigma_0}{E}=\varepsilon_{el}+0.002 \tag{4}$$

Fitting data in Figure 4 of two samples of dental CoCrMo alloy using a least-squares method, the material parameters of nonlinear Ramberg-Osgood equation (3) were found and shown in Table 2.

Table 2: *Ramberg-Osgood's material parameters of dental CoCrMo alloy*

Specimen	α	n	R^2
1	0.527	13.02	0.976523
2	0.453	15.43	0.978425

The Ramberg-Osgood's material curve of dental CoCrMo alloy was shown with the averaged values of the strain hardening parameter n=14.225 and a comparison with the curves obtained by the static tensile test is shown in Fig. 6.

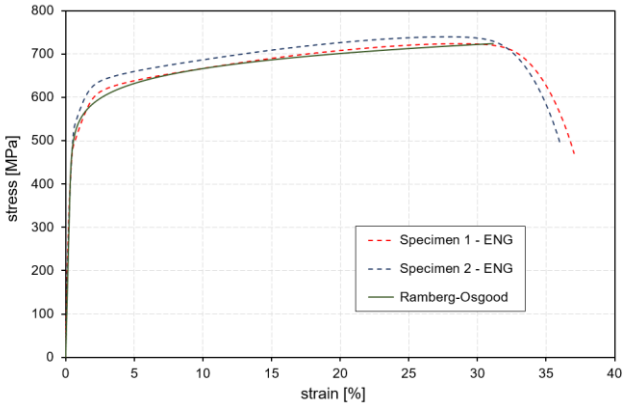

Fig. 4 *Comparison of Ramberg-Osgood's and engineering stress-strain diagrams of dental CoCrMo alloy*

3. Determination of plastic zone magnitude around the crack tip

The best approximation of the nonlinear distribution of the cohesive stresses [2,4] is achieved by the analytical expression

$$p(x)=\sigma_0\left(\frac{r_p}{x-a}\right)^{1/(n+1)} \tag{5}$$

The physical quantity $p(x)$ (see Fig. 1c) is a function of the two parameters, i.e. r_p and n. The stress intensity coefficient K and the magnitude of the plastic zone around a crack tip r_p can be determined by using the method of weight functions (Green's function). The Green's function for an infinite cracked plate, loaded on stretching in a direction perpendicular to the crack plane, according to D. Pustaić [6] amounts

$$m(x,b)=2\sqrt{\frac{b}{\pi}}\left(b^2-x^2\right)^{-1/2} \tag{6}$$

The stress intensity coefficient can be calculated using Green's function [2, 7], knowing the distribution of the cohesive stresses (7), as

$$K_{coh}(b)=\int_a^b p(x)\cdot m(x,b)\,\mathrm{d}x \tag{7}$$

Introducing a new variable ξ, according to [2], the variable x has the form $x = a + r_p(1-\xi) = b - r_p\xi$ ($\xi = 1$ for $x = a$, and $\xi = 0$ for $x = b$), the expression (7) is transformed in the following form

$$p(\xi) = \sigma_0 (1-\xi)^{-1/(n+1)} \tag{8}$$

Inserting the expressions (6) and (8) in (7) and after arranging the following expression is obtained

$$K_{\mathrm{coh}}(b) = \sqrt{\frac{2}{\pi} r_p} \cdot \sigma_0 \int_0^1 \frac{1}{(1-\xi)^{1/(n+1)}} \cdot \frac{1}{\left[\xi\left(1-\frac{r_p}{2b}\xi\right)\right]^{1/2}} \mathrm{d}\xi \tag{9}$$

By forming the above expression the assumption about the small crack tip plastic zone can be introduced. Under small-scale yielding (SSY) conditions it could be taken $r_p / 2b \approx 0$. After integration, the final result for $K_{\mathrm{coh}}(b)$ has the form

$$K_{\mathrm{coh}}(b) = \sqrt{\frac{2}{\pi} r_p} \cdot \sigma_0 \frac{\Gamma\left(\frac{1}{2}\right) \cdot \Gamma\left(\frac{n}{n+1}\right)}{\Gamma\left(\frac{1}{2}+\frac{n}{n+1}\right)} = \sqrt{\frac{2}{\pi} r_p} \cdot \sigma_0 B\left(\frac{1}{2}, \frac{n}{n+1}\right) \tag{10}$$

where $\Gamma(x)$ stands for the gamma function or the Euler's integral of the second type and $B(x, y)$ is the beta function or the Euler's integral of the first type. This result must be taken with the opposite sign because the stress intensity coefficient $K_{\mathrm{coh}}(b)$ takes the negative value if calculations are being conducted for the direction of the cohesive tensile stresses. The stress intensity coefficient, corresponding to a remote tension of a plate with an imaginary crack of length b, amounts to

$$K_{\mathrm{ext}}(a + r_p) = \sigma_\infty \sqrt{\pi (a + r_p)} \,. \tag{11}$$

By equating the right sides of the expressions (10) and (11) and by arranging that equation, the magnitude of plastic zone r_p in front of the crack tip [7], normalized to the initial crack length a, by an assumption of the small plastic zone, is obtained as

$$\frac{r_p}{a} = \frac{\pi}{2}\left(\frac{\sigma_\infty}{\sigma_0}\right)^2 \cdot \frac{\left[\Gamma\left(\frac{1}{2}+\frac{n}{n+1}\right) \Big/ \Gamma\left(\frac{n}{n+1}\right)\right]^2}{1 - \frac{\pi}{2}\left(\frac{\sigma_\infty}{\sigma_0}\right)^2 \cdot \left[\Gamma\left(\frac{1}{2}+\frac{n}{n+1}\right) \Big/ \Gamma\left(\frac{n}{n+1}\right)\right]^2} \tag{12}$$

4. Results and discussion

On the basis of analytical expression (12), the values of plastic zone magnitude r_p in front of the crack tip, normalized to the initial crack length a, are calculated in dependence upon monotonously increasing external load σ_∞/σ_0, for dental CoCrMo alloy. The results were obtained by means of the commercial software package *Mathematica* and presented in the form of diagrams in Fig. 5.

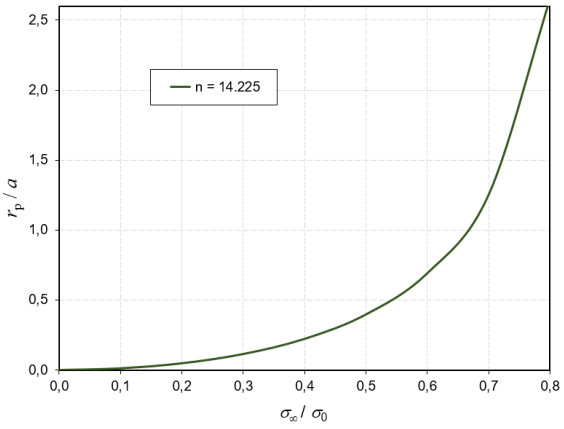

Fig. 5 *Dependence of plastic zone magnitude r_p on load σ_∞/σ_0 of dental CoCrMo alloy*

The results of the magnitude of plastic zone r_p in Fig. 5 are presented as a function of the external load which is normalized to 0.2% offset yield stress (σ_∞/σ_0). This display of results in the non-dimensional form includes only the strain hardening parameter n of the Ramberg-Osgood equation for dental CoCrMo alloy.

From the diagram in Fig. 5, it can be seen that the magnitude of the plastic zone at the crack tip does not increase linearly with the external load of the thin plate. If we assume that the crack is 20 mm (a=10mm), the size of the plastic zone at the crack tip in the direction of the x-axis according to Fig. 1 at an external load of 100MPa (σ_∞/σ_0=0.2) is 0.47mm, while at 200MPa (σ_∞/σ_0=0.4) it is 2.22mm. That's an increase in the magnitude of the plastic zone at the crack tip by 372%. With a higher external load, the magnitude of the plastic zone at the crack tip is larger.

5. Conclusion

The aim of this investigation was to establish if, and, in what measure the isotropic hardening of the dental CoCrMo alloy influences the magnitude of the plastic zone around the crack tip. The goal was to develop the corresponding analytical expressions for calculating the r_p and not to use the numerical methods. One well-known cohesive model for the crack analysis was applied. The non-singularity condition of the stress distribution at the tip of the fictitious elastic crack is noted in the form (1). In this paper, the analytical expression (5) for the distribution of the cohesive stresses is taken. On the basis of analytical expression (12), the values of plastic zone magnitude r_p in front of the crack tip, normalized to the initial crack length a, are calculated in dependence upon monotonously increasing external load σ_∞/σ_0, for dental CoCrMo alloy. The results were obtained by means of the commercial software package *Mathematica* and presented in the form of diagrams in Fig. 5. From the diagram in Fig. 5, it can be seen that the magnitude of the plastic zone at the crack tip increase non-linearly with the external load of the thin plate.

Acknowledgments: Investigations were performed within research project IP-124 University of Zagreb Faculty of Metallurgy, Centre for Foundry Technology—SIMET, KK.01.1.1.02.0020 and VIRTULAB—Integrated laboratory for primary and secondary raw materials, KK.01.1.1.02.0022.

6. References

1. B. Li, A. Mukasyan, A.Varma, Mater. Res. Inovations, **7**, 4 (2003).
2. X.G. Chen, X.R. Wu, M.G Yan, Eng. Fract. Mech., **41**, 6 (1992).
3. M. Hoffman, T. Seeger, Dugdale Solutions for Strain Hardening Materials. The Crack Tip Opening Displacement in Elastic-Plastic Fracture Mechanics. In: Proceedings of the Workshop on the CTOD Methodology, 57-77. Geesthacht, (1985).
4. A. Neimitz, Eng. Fract. Mech., **71**, 11 (2004).
5. P.S. Patwardhan, R.A. Nalavde, D. Kujawski, Procedia Struct. Integrity, 17 (2019).
6. D. Pustaić, M. Lovrenić, Analytical and Numerical Investigation of Crack Opening in Strain-Hardening Material. In: *Proceedings of 5th International Congress of Croatian Society of Mechanics* and CD-ROM, Croatian Society of Mechanics. Croatia, Trogir (2006).
7. D. Pustaić, M. Lovrenić-Jugović, Mathematical Modeling of Cohesive Zone in the Ductile Metallic Materials. In: *Proceedings of the 9th International Congress of Croatian Society of Mechanics*. Croatian Society of Mechanics. Croatia, Split (2018).

Nanophase structures in vacuum multilayer coatings formed on tool and high-speed steels

Yauheni Auchynnikau[1], Nikolai Chekan[2], Gennady Kostukovich[1], Igor Akula[2], Alexander Ogorodnikov A.[3]
Faculty of Innovative Mechanic Engineering [1], Faculty of Engineering and Construction [3] – Yanka Kupala State University of Grodno, Belarus
Department of thin films and coatings - Physical-Technical Institute of the National Academy of Sciences of Belarus [2]

Abstract: *The most common coatings for metalworking tools include titanium nitride, titanium carbide, titanium carbonitride, zirconium nitride, zirconium carbide, zirconium carbonitride, compounds based on chromium, titanium, aluminum, diamond-like coatings that are formed in vacuum using PVD, CVD, PCVD methods or a combination of the above methods. The current trend in the deposition of vacuum coatings is the production of multifunctional coatings, which can significantly increase operational characteristics compared to the starting materials. To form multifunctional coatings, the creation of "sandwich" structures is used, since each layer performs various functions - forming, antiwear, anticorrosion. Thus, the use of a composite multilayer coating containing layers of titanium nitride, titanium, diamond-containing compounds with a thickness of one layer from 0.1 to 2 microns makes it possible to increase the wear resistance of a metalworking tool by 1.5-5 times.*

KEYWORDS*: MORPHOLOGY, DIAMOND-LIKE COATINGS, PROPERTIES, STRUCTURE.*

1. Introduction

Coatings of diamond-like carbon (DLC) have a whole range of necessary tribological characteristics, the main of which are high hardness, low values of the friction coefficient, and chemical inertness. However, it is well known that the tribological properties of DLC coatings—whether hydrogenated (a-C:H) or non-hydrogenated (a-C)—are highly dependent on the operating conditions of the medium. The mechanism responsible for this effect is probably associated with the interaction of carbon with uncompensated bonds in gas phase particles, for example, water. Consequently, the use of conventional DLC coatings may not be applicable when extreme or labile operating conditions are expected, as in internal combustion engines, turbines, which must operate in both high and low temperatures, humidity. In this connection, there was a nanocomposite coating consisting of nanoparticles of solid WC and solid lubricant WS_2 embedded in a non-hydrogenated matrix. DLC principles have been described in a number of works. According to data available in the literature, coatings based on tungsten carbides in combination with titanium and cobalt are significantly less sensitive to environmental influences. The combination of DLC coatings and coatings based on tungsten carbide will significantly change the tribological and corrosion characteristics of the formed multifunctional coatings. However, most works do not consider the formation of nanocomposite structures in multilayer coatings based on systems modified tungsten carbide - APP. Nanocomposite coatings with a microstructure consisting of nanocrystalline grains in an amorphous matrix of a diamond-like coating must have unique mechanical and tribological parameters. Thus, it is possible to create superhard coatings with microhardness values of ~50–55 GPa, i.e. nanocomposite coatings were created in which plastic deformation was reduced in order to increase hardness. This mechanism for reducing the deformation strength can be carried out due to grain boundary and dispersion strengthening. Materials with low ductility are quite brittle.

Therefore, they are not ideal for applications where high contact stresses occur, such as plain bearings, where high wear resistance and ductility as well as a low coefficient of friction are required. There are publications that show the creation of good ductile properties in brittle ceramics at room temperature by reducing the grain size to the nanometer level. This approach will make it possible to obtain good tribological characteristics of nanocrystalline oxides of various materials [1-4].

2.1. Preconditions and means for resolving the problem

Further work in this direction showed the promise of including nanocrystalline ceramic grains in a lubricating matrix (if this system is considered as a tribological one), such as coatings based on amorphous carbon (a-C). As a rule, the technologies used for the production of nanocrystalline / amorphous composite coatings lead to the heating of the substrate to a temperature of about 500–600 ° C, which is due to the ongoing processes of the formation of a crystalline phase in the coating. On the other hand, this temperature range can significantly limit the choice of substrate material and reduce the benefits of creating protective coatings. Moreover, at these temperatures, the sp^3 hybridization of bonds in carbon atoms in DLC coatings, which causes high hardness, can pass into a graphite-like phase with a bond of sp^2 hybridizations. Thus, it is necessary to develop other methods for the implementation of crystal formation processes in composite DLC coatings with a-C solid matrix. It is possible to carry out the formation of carbide and carbonitride crystals by sharing a low-energy metal plasma formed by magnetron sputtering with high-energy torches created by pulsed laser ablation of graphite. This technology is Magnetron Pulsed Laser Deposition (MPLD), it can also be used to deposit TiC, TiCN, Hydrogen-Free A-C DLC coatings. The obtained coatings TiC and APP (a-C) have a very high hardness of 27 and 60 GPa, respectively. In addition, the APP coating (a-C) had low friction coefficient values of less than 0.1 under most tribological test conditions. During the formation of this composite coating, a transition of coatings Ti –> APP was observed, with the formation of an intermediate layer according to the scheme Ti → TiC → APP (a-C). This process occurred with an increase in the carbon content. Studies have shown that even when the deposition process is carried out at a temperature of 100 °C, a two-phase TiC → APP region is formed. This approach is used in obtaining the production of nanocrystalline composite coatings TiC / APP (a-C). Thus, the approach of forming multilayer coatings is quite promising for obtaining multifunctional coatings, due to the formation of thin-layer systems of nanocrystalline particles and phases in the structure. Figure 1-8 shows the results of atomic force microscopy of DLC coatings formed on steel substrates of the M2 (HSS) and H13 types.

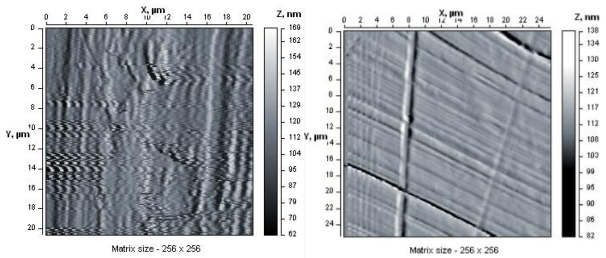

a) b)

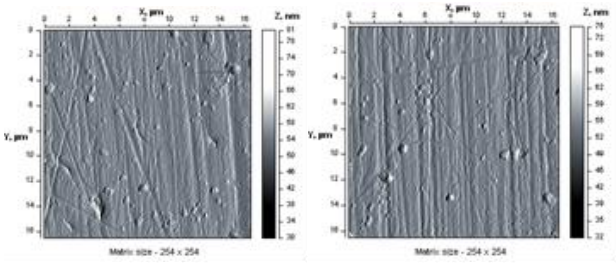

c) d)

Figure 1 *- Morphology of the surface layers of vacuum coatings formed on carbon and high-speed steels (2D image): a - original steel H13, b - original steel HSS; v-steel H13 with a diamond-like coating; g - HSS steel with a diamond-like coating.*

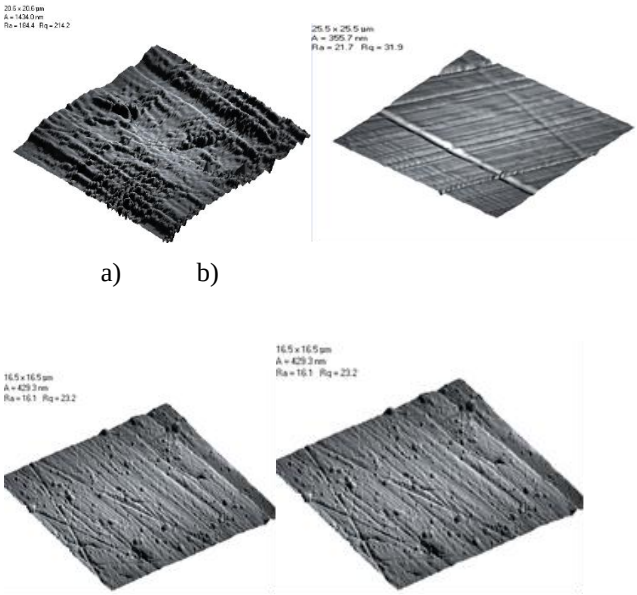

a) b)

c) d)

Figure 2 *- Morphology of the surface layers of vacuum coatings formed on carbon and high-speed steels (3D image): a - original steel 4Kh5MFS, b - original steel R6M5; v-steel 4Kh5MFS with a diamond-like coating; g - R6M5 steel with a diamond-like coating.*

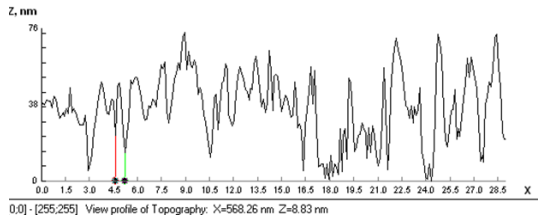

a)

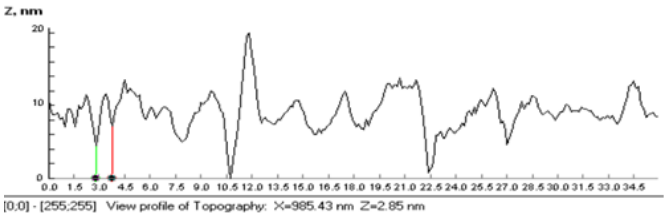

b)

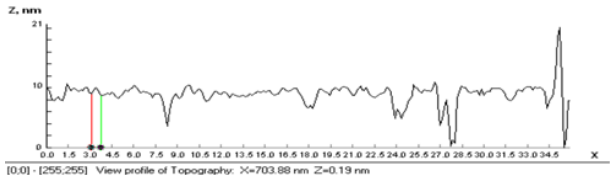

c)

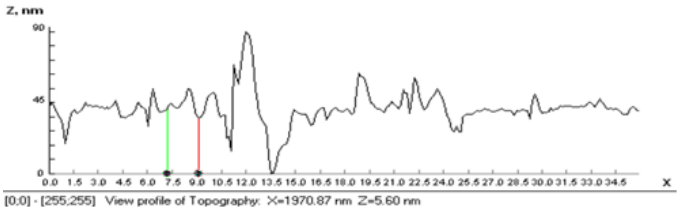

d)

Figure 3 *- Topography of the surface layers of vacuum coatings formed on carbon and high-speed steels): a - original steel H13, b - original steel HSS; v-steel H13 with a diamond-like coating; g - HSS steel with a diamond-like coating.*

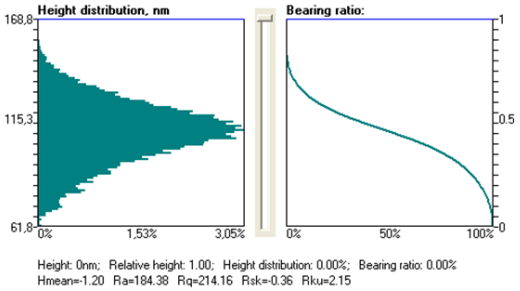

a)

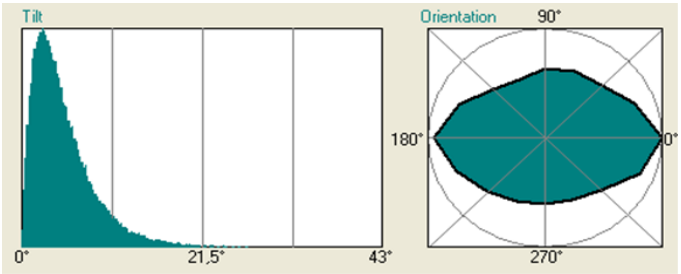

b)

Figure 4 *- The main characteristics of the morphology of the surface layers of steel H13. a-distribution by heights; b-angular distribution*

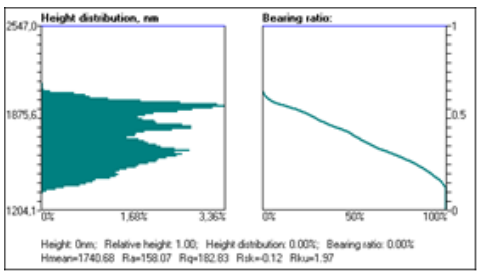

a)

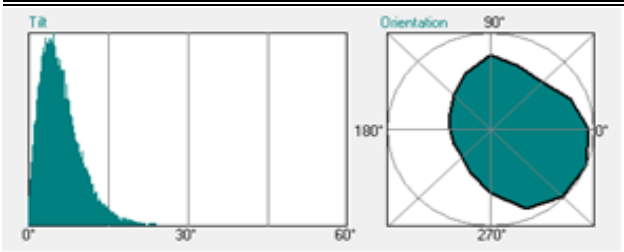

b)

Figure 5 *- The main surface characteristics of steel HSS: a-height characteristic, b-angular distribution.*

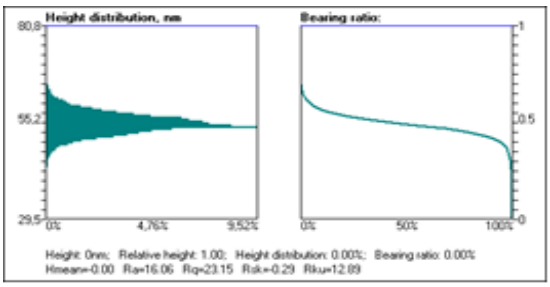

a)

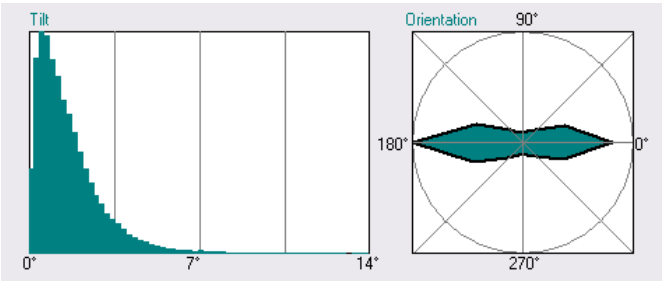

b)

Figure 6. The main surface characteristics of steel H13 with a diamond-like coating: a-height characteristic, b-angular distribution.

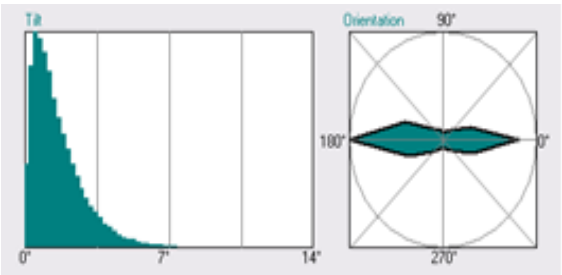

a)

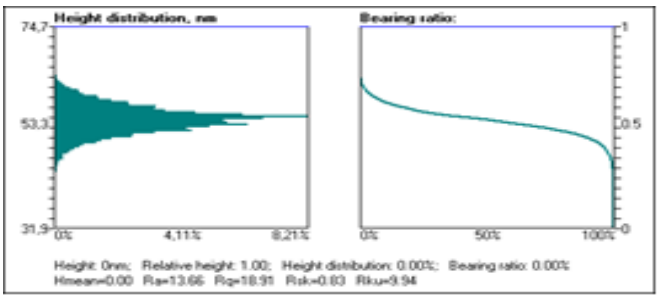

b)

Figure 7 *- The main surface characteristics of HSS steel with a diamond-like coating: a-height characteristic, b-angular distribution.*

Based on the presented data, it can be seen that nanodispersed structures begin to form in diamond-like coatings when they are deposited on the surface of steel substrates. This process is intensified during the formation of APP on superhard layers deposited on steel substrates (Figure 8).

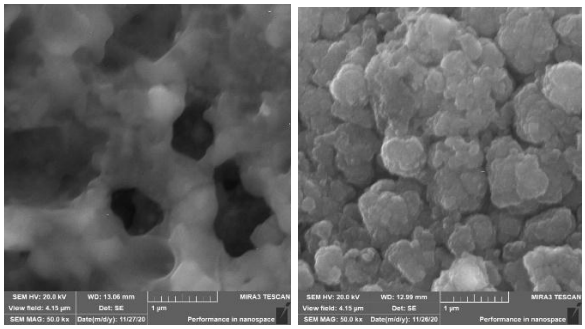

a) b)

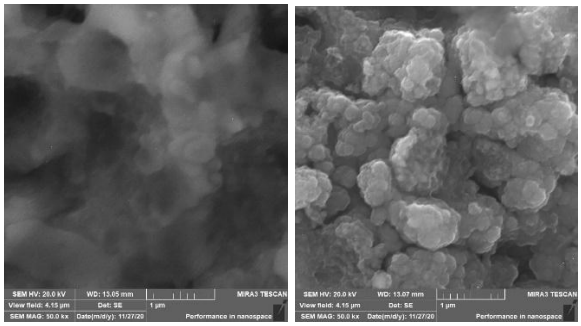

c) d)

Figure 8 *- Morphology of APP coatings formed on superhard sublayers of HSS and H13 steel substrates. a - HSS substrate, VK6 sublayer, Norma 1 sublayer formation mode, b – H13 substrate, VK6 sublayer, Norma 2 sublayer formation mode, c - HSS substrate, VK6 sublayer, Norma 1 sublayer formation mode, b – H13 substrate, VK6 sublayer, sublayer formation mode Norma 2*

The most common coatings for metalworking tools include titanium nitride, titanium carbide, titanium carbonitride, zirconium nitride, zirconium carbide, zirconium carbonitride, compounds based on chromium, titanium, aluminum, diamond-like coatings that are formed in vacuum using PVD, CVD, PCVD methods or a combination of the above methods. The current trend in the deposition of vacuum coatings is the production of multifunctional coatings, which can significantly increase operational characteristics compared to the starting materials. To form multifunctional coatings, the creation of "sandwich" structures is used, since each layer performs various functions - forming, antiwear, anticorrosion. When using a cutting tool with multilayer and composite coatings, the stability of the cutting tool and its performance characteristics change radically, wear is reduced, cutting accuracy is increased, it becomes possible to increase the feed, the quality of surface treatment increases and tool durability increases. Thus, the use of a composite multilayer coating containing layers of titanium nitride, titanium, diamond-containing compounds with a thickness of one layer from 0.1 to 2 μm makes it possible to increase the wear resistance of a metalworking tool by 1.5-5 times. Creation of multilayer vacuum coatings, including those containing nanophases and nanoparticles in their structure, using multicomponent magnetically controlled flows of metal and carbon plasma, of the following composition: (Al-Ti-Cr-Si)-(C, N), CN, CF, CB , will significantly increase the physical and mechanical properties of the modified products. It has been established that the formation of vacuum coatings on a modified steel surface by the method of electrospark alloying also leads to a decrease in the surface roughness values of the modified steel substrate.

Thus, the formation of nanocomposite structures in multifunctional coatings depends on the type of sublayer material, as well as on the modes of coating formation

References:

1. Ti-Al-N hard coatings deposited from filtered vacuum-arc plasma / V.V. Belous [et al.] // Physical engineering of the surface. -2009. - v. 7, No. 3. -S. 216-220.

2. Ovchinnikov, E.V. Tribotechnical characteristics of AlTiN plasma-chemical coatings / E.V. Ovchinnikov, N.M. Chekan, I.P. Akula // Fundamental and applied problems of engineering and technology. - 2014. - No. 1 (303). - S. 55-63.

3.Adhesive activity AITiN layers based on forming polymer coatings / Y. Auchynnikau [et al.] // The proceedings of the Austrian-Slovenian Polymer Meeting 2013 [Elektronski vir] / Austrian-Slovenian Polymer Meeting-ASPM 2013, 3-5 April 2013, Bled, Slovenia; editors Majda Žigon, Teja Rajšp.- El. zbornik. - Ljubljana: Centre of Excellence PoliMaT, 2013. – P. 256- 257.

4. Obtaining and heat treatment of coatings of the Ti-Al-Si-N system / N.M. Coinage [et al.] // Bulletin of the State Duma, ser. 6. - 2013. - No. 2 (154). - S. 31-37. 4. N.M. Chekan [et al.] // Vesník GrDU, ser. 6. – 2013. – № 2 (154). – P. 31-37.

Features of the tribological behavior of the magnesium alloy Mg -1% ca depending on the structural state

Vladimir I. Semenov [a+], Hsin-Chih Lin [b], Sergey V. Chertovskikh [a], Olga B. Kulyasova [a, c]

[a] Ufa State Aviation Technical University,
12 K. Marx St., Ufa 450008, Russia.
[b] National Taiwan University
1, Roosevelt Road, Sec. 4, Taipei 106, Taiwan R.O.C.
[c] Bashkir State University,
32 Zaki Validi St., Ufa 450076, Russia
[+]corresponding author, e-mail: semenov-vi@rambler.ru

Abstract: *This paper presents experimental data on the tribological properties of the Mg-1%Ca magnesium alloy with different microstructures (coarse-grained microstructure in the initial state, and ultrafine-grained and nanocrystaline microstructures after severe plastic deformation via two processes – equal-channel angular pressing and high pressure torsion) in contact with an indenter made of the Fe-18W-4Cr-0.8C steel without any coating and with applied hydroxyapatite, which is the main mineral component of bones. An indenter with hydroxyapatite on the surface was used as a bone simulator. As a result of the experiments, it was found that the shear strength of adhesive bonds and the adhesive component of the friction coefficient are structurally sensitive parameters. For all the samples in the considered contact pairs, when using a bone tissue simulator the strength of adhesive bonds was lower than that when using a steel indenter. It is noted that ultrafine-grained and nanocrystalline structures produced as a result of severe plastic deformation via two processes, equal-channel angular pressing and high pressure torsion, contribute to a decrease in the shear strength of adhesive bonds and the adhesive component of the friction coefficient due to strengthening resulting from grain size reduction from originally 100 μm to 1.4–4 μm on average in the investigated Mg-Ca magnesium alloy.*

KEYWORDS: *STRENGTH OF ADHESIVE BONDS, ADHESIVE COMPONENT OF THE FRICTION COEFFICIENT, SEVERE PLASTIC DEFORMATION, HYDROXYAPATITE.*

1. INTRODUCTION

In [1, 2], a brief review of modern scientific literature on the main achievements and problems of biomedical magnesium alloys for traumatology and orthopedics is presented. Great interest in these materials is due to the fact that magnesium alloys are highly biocompatible, bioinert, hypoallergenic and, moreover, non-toxic [3, 4]. The disadvantage of magnesium alloys with a coarse-grained (CG) structure is its low strength. To increase the strength and functional properties of Mg alloys, rather widely used is alloying with different elements [5–8]. Such a method for increasing strength is quite efficient, but is not always acceptable for materials intended for the use in medical implants due to the possible adverse effects of some alloying elements on the human body.

According to expert evaluation, it is promising to use Mg-Ca magnesium alloys in medical implants for osteosynthesis [9], since both of these chemical elements are present in bone tissue and have a beneficial effect on the body. It has been found that the presence of Ca in a Mg alloy normally reduces its strength and ductility at room temperature. As noted in [10], the effect of Ca is not so unambiguous. Although the offset yield strength increases from 30–35 MPa for pure Mg to about 95 MPa for the Mg-0.9 Ca alloy, elongation decreases from 10–12% to 2–3%, respectively.

The applied technologies of deformation treatment make it possible to achieve a high-strength state due to the formation of an ultrafine-grained (UFG) and nanocrystalline (NC) microstructure, which contributes to an increase in mechanical and functional properties [11]. Severe plastic deformation (SPD) methods, in particular, equal-channel angular pressing (ECAP) and high pressure torsion (HPT) [12, 13, etc.] due to the formation of UFG and NC structures, enable increasing the strength of alloys by 20-60% while preserving a rather high ductility (about 8–10%).

Currently, magnesium alloys are used as load-bearing implants, such as plates, screws and pins, to repair bone fractures. Degradable coronary stents are an important area of research. Degradable vascular stents contribute to the stable regeneration of vessels, in contrast to permanent stents [14].

It is known that in many conjugations that are in a mobile or static contact, the tribological [15, etc.] and adhesive [16, 17] interactions of surfaces play an important role and are among the main functional properties in implantology during osteosynthesis. In this case, the adhesive interaction can activate the processes of corrosion and dissolution of protective films and coatings. The authors plan further research in this area in the future.

A number of papers [18-20, etc.] are devoted to the problem of evaluating the shear strength of adhesive bonds. However, the presented papers lack practically any analysis into the effect of microstructure on the tribological properties of a Mg-Ca magnesium alloy contacting bone tissue, where one of the main components in hydroxyapatite. Besides, it is known than bones serve as a magnesium depot in the body [21], which is of practical interest in terms of the contact interaction between Mg-containing implants and bone tissue.

It follows from the given analysis that the issues of adhesive interaction between implants made of a Mg-Ca magnesium alloy with different microstructures and bone tissue have not yet been sufficiently studied. At the same time, these issues are important for understanding various phenomena related to the bioresorption time (speed) of these materials and call for further study [14].

Thus, the aim of this paper is a comparative evaluation of the adhesive interaction with a Mg-Ca magnesium alloy having different microstructures (coarse-grained one in the initial state after casting, preliminary extrusion and annealing, and UFG/NC one after SPD processing) in the contact pairs “magnesium alloy – steel” and “magnesium alloy – bone tissue” to reveal the potential of the deformation treatment of the material under study.

A contribution to solving this set task is of scientific and practical interest. The novelty of the proposed tribological studies with the evaluation of the strength of adhesive bonds is that it is practically the first time such studies are conducted for a Mg-Ca magnesium alloy, and that they may be used when designing processes for the production of next-generation medical implants.

2. RESEARCH METHODS AND MATERIALS

As the material for the study, we used the low-alloyed, specially manufactured in a laboratory, Mg-1%Ca magnesium alloy with a coarse-grained (CG) structure after casting and preliminary extrusion, with UFG/NC microstructures after SPD processing by ECAP and HPT. The microhardness of the samples in the initial as-extruded condition was 53.3 ± 3 HV, after ECAP processing – 71,1 ± 4 HV, and after HPT processing – 98 ± 5 HV. The roughness of the contact surfaces, *Ra*, was about 1.6.

For the tribological studies aimed at finding the shear strength of adhesive bonds and the adhesive component of the friction coefficient, a single-ball adhesion tester was used. The test principle is shown in Fig. 1.

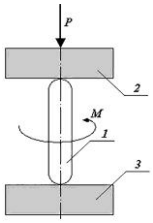

Fig. 1. Principle of the test to find the shear strength of adhesive bonds and the molecular component of the friction coefficient: 1 is a spherical indenter; 2 and 3 are test samples

The presented principle was used to evaluate the shear strength of adhesive bonds and the adhesive component of the friction coefficient. The test samples were in the form of disks with a diameter of 25 mm and a thickness of 5 mm. The spherical indenter with a sphere radius of 2.5 mm was made of the Fe-18W-4Cr-0.8C high-speed steel. The normal load was 1500 N.

The tests were carried out at room temperature (25°C) according to the method described in [22]. This method is based on a physical model which in the first approximation reflects the real conditions of friction at a local contact.

According to this model, the spherical indenter 1, compressed by two plane-parallel samples 2 and 3, rotates under a load around its own axis. The force F spent on the rotation of the indenter is mainly related to the shear strength of adhesive bonds, τ_n.

The shear strength of adhesive bonds, τ_n (MPa), was determined from the ratio:

$$\tau_n = 0.75 \cdot \frac{M}{\pi \cdot \left(\frac{d_{1,2}}{2}\right)^3}, \quad (1)$$

where $d_{1,2}$ are the diameters of imprints on the test samples, mm; *M* is the indenter's torque, *N mm*.

The adhesive (molecular) component of the friction coefficient was determined from formula (2) as the relation of the strength of adhesive bonds to normal pressure:

$$f_M = \frac{\tau_n}{p_r}, \quad (2)$$

where p_r *is* normal pressure, *MPa,*

$$p_r = \frac{P}{\pi \cdot \left(\frac{d_{1,2}}{2}\right)^2} \quad (3)$$

where *P* is the compressive force of the samples, *N.*

The contact surfaces of the indenter and the samples in different structural states were prepared for the comparative tribological tests in the following manner: in the first case – in a clean form (after degreasing) and in the second case – with an applied hydroxyapatite (HA) suspension. HA was used as a material imitating bone tissue. The suspension was applied onto the contact surfaces of the indenter 1 and the test samples 2 (Fig. 1).

As noted above, the test samples had CG and UFG/NC microstructures produced, in the first case, as a result of casting, extrusion and annealing at 250 °C for 1.5 hours, and in the second case, as a result of SPD processing by ECAP and HPT. The principles of the SPD processes are shown in Fig. 2.

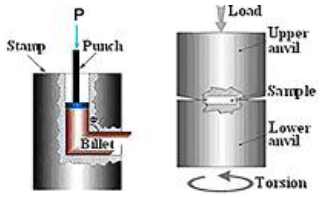

a *b*

Fig. 2. Equipment and die-set for SPD processing: *a* –ECAP processing; *b* – HPT processing

ECAP processing for 8 cycles (Fig. 2 *a*) was performed via route Bc route with 90° rotation around the longitudinal axis of the billet after each processing cycle. The cross-member speed was 6 mm/s. The channels intersection angle was 120°. 4 cycles were performed at a temperature of 250 °C and the following 4 cycles – at a temperature of 230 °C.

HPT processing (Fig. 2 *b*) was performed at room temperature under a normal pressure of 6 GPa at a speed of 1 rpm with a total number of revolutions of 10. The samples for HPT were in the form of disks with a diameter of 20 mm and a thickness of 1 mm.

Metallographic studies were carried out using an Olympus GX51 optical microscope, a JEM-6390 scanning electron microscope (SEM), and a JEM-2100 transmission electron microscope (TEM) with accelerating voltages of 10 kV and 200 kV.

3. RESULTS OF METALLOGRAPHIC STUDIES

Fig. 3 shows an image of the microstructure of the Mg-1%Ca alloy after extrusion. The intermetallic compound Mg2Ca separated during extrusion into small particles which became uniformly distributed. Based on this observation, it can be stated that the presence of small particles in grain interiors will lead to a significant increase in the mechanical properties of the Mg-1%Ca alloy [23, 24].

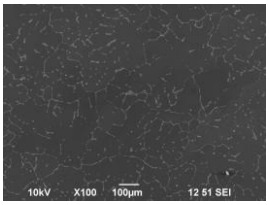

Fig. 3. SEM image of the Mg-1%Ca alloy after extrusion

In order to produce bulk billets, the ECAP method was applied to the extruded samples. A typical view of the samples after ECAP processing is shown in Fig. 4 *a*.

After ECAP processing, the alloy contains Mg_2Ca particles with a size of 2-3 μm, arranged in lines (Fig. 4 *b*). Microstructural studies of the Mg-1%Ca alloy samples after ECAP processing revealed an average α-Mg grain size of 4 μm and the presence of particles of the Mg_2Ca second phase with a volume fraction of 3% (Fig. 4 *b, c*). Study by TEM revealed a high density of dislocations (Fig. 4 *d, e*) and the presence of twins in the structure, 500 nm in width and up to several microns in length (Fig. 4 *d*).

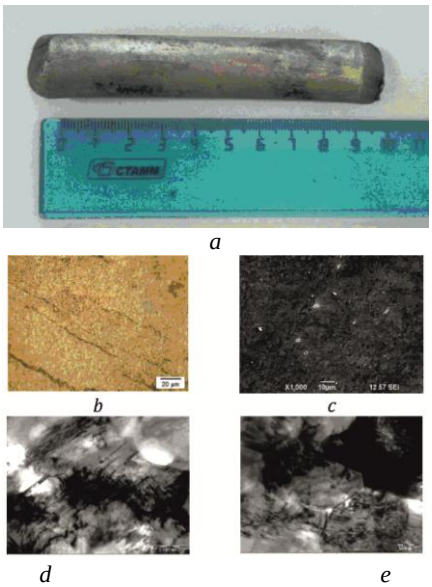

Fig. 4. View of a billet and the microstructure of the Mg-1%Ca alloy after ECAP: *a* – view of the sample after ECAP; *b* – Mg_2Ca particles with a size of 2-3 μm, arranged in lines; *c* – particles of the Mg_2Ca second phase; *d* – twins in the structure; *e* – dislocations.

Study by SEM of the structure of the samples after HPT processing and additional annealing at 250 °C revealed the presence in the structure of particles and eutectics with a total volume fraction of 4.0% (Fig. 5 *a*). According to the SEM images, the average grain size is 1.4 μm.

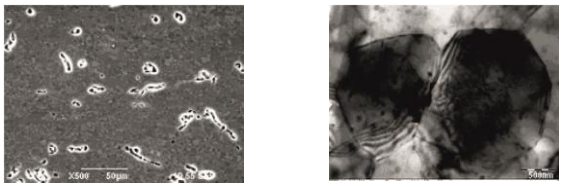

Fig. 5. Microstructure after HPT (*a*) and additional annealing at 250 °C (*b*).

The structure contains particles that obviously formed during the decomposition of the supersaturated solid solution formed in the process of HPT (Fig. 5 *b*).

4. RESULTS OF TRIBOLOGICAL TESTS

Fig. 6 shows the imprints of the indenter on the surface of the test material, obtained during tribological tests to determine the shear strength of adhesive bonds and the adhesive component of the friction coefficient. Samples of the magnesium alloy had different microstructures and differently treated contact surfaces.

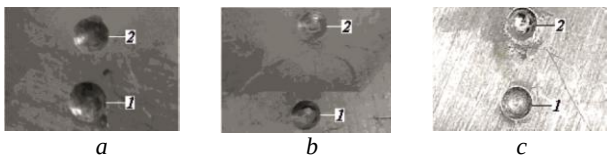

Fig. 6. Imprints of the indenter on the surface of the test samples: *a* – the initial state of the test material with a CG structure; *b* – sample after ECAP with a UFG structure; *c* – sample after HPT with UFG and NC structures. Index 1 corresponds to the degreased contact surface, index 2 – to HA applied onto the contact surface. 10x magnification.

As it can be seen in Fig. 6 *a*, the imprints of the indenter on the surface of the material in the initial (coarse-grained) state are somewhat larger in comparison to those in the SPD-processed material (Fig. 6 *b*, *c*). This indicates the lower strength of the material with a coarse-grained structure. As noted in [25-27], SPD processing leads to the formation of a structural and phase state that ensures a higher strength. In this case, there are two mechanisms responsible for a higher strength after SPD processing, namely grain-boundary strengthening, since the length of grain boundaries is larger at a smaller mean grain size, precipitation hardening expressed in dispersed particles of the second phase, as well as strengthening due to the accumulation of a high dislocation density. In addition, it was noted that the diameters of the indentation cups practically do not depend on the presence or absence of hydroxyapatite on the contact surfaces of the investigated triboconjugations. In this case, this speaks of the decisive role of the rheological properties of the investigated material itself – the Mg-1%Ca magnesium alloy.

The results from finding the shear strength of adhesive bonds in the friction pairs "Mg-1%Ca magnesium alloy – *Fe-18W-4Cr-0.8C* high-speed steel" in a clean form after degreasing and with HA applied onto the contact surfaces of the indenter and the test samples are shown in Fig. 7.

In order to increase the reliability of the test results, during the tribological studies three duplicating tests (loading of the test samples with an indenter) were performed, measuring the imprint diameters and averaging the measurement results with a subsequent statistical processing of the values of the shear strength of adhesive bonds [28]. The diagrams shown in Fig. 7 correspond with 95% probability to the 5% confidence interval of significant values, which enabled approximating the obtained values as direct lines.

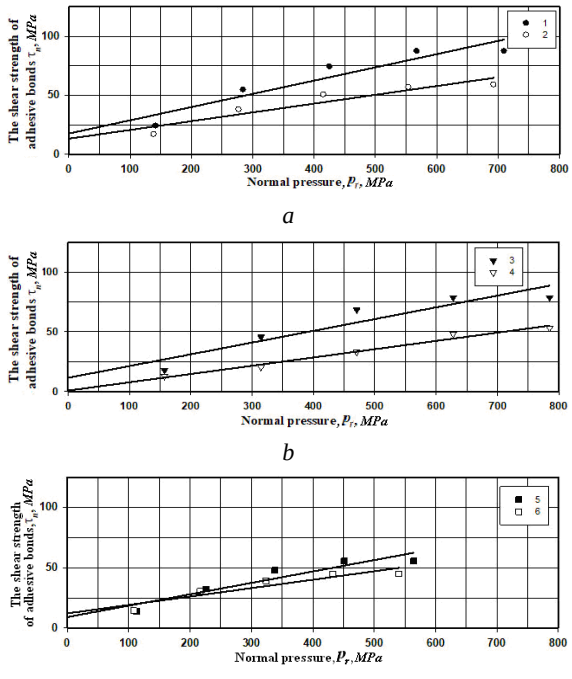

Fig. 7. Dependence of the shear strength of adhesive bonds on the normal stress at the contact:
a – 1 – the initial state of the tested material with a CG structure, the contact surfaces are degreased; 2 – the initial state of the tested material with a CG structure, HA is applied onto the contact surfaces;
b – 3 – samples after ECAP with a UFG structure, contact surfaces are degreased; 4 – samples after ECAP with a UFG structure, HA is applied onto the contact surfaces;
c – 5 – samples after HPT with UFG and NC structures, contact surfaces are degreased;
6 – samples after HPT with UFG and NC structures, HA is applied onto the contact surfaces.

As it can be seen from the dependencies presented in Fig. 7 (*a*, *b*, *c*), the values of the shear strength of adhesive bonds and the adhesive component of the friction coefficient, under the experimental conditions, tend to decrease with increasing strength of the Mg-1%Ca magnesium alloy, evidently due to grain size reduction after the deformation treatment [12, 13] and the presence of a bone tissue simulator in the form of hydroxyapatite suspension on the contact surfaces. At the same time, analyzing the tribological behavior of each pair of test samples with the same structure, but in the presence and absence of hydroxyapatite in the triboconjugation, it was noted that, within the experiment error, the load-bearing capacity remains practically constant. This is visibly illustrated in Fig. 7 by the length of the branch of each presented diagram. For example, in diagrams (*a* - 1 and 2), (*b* - 3 and 4), (*c* - 5 and 6) in each of the examined tribological pairs the branch length varies insignificantly. This may indicate that the load-bearing capacity of the investigated material (Mg-1%Ca) depends primarily on the rheological properties of the investigated material, which in their turn are determined by microstructure.

Table 1 shows the complete results of the tribological tests to determine the shear strength of adhesive bonds and the adhesive component of the friction coefficient.

Table 1. Results of tribological tests.

Material (line number in Fig. 7)	p_{rn}, MPa	τ_n, MPa	τ_n/p_r	β^*	τ_0^*, MPa
Mg - 1% Ca in the initial state, Fe-18W-4Cr-0.8C indenter (contact surfaces are degreased) **(1)**	710	97.2	0.14	0.11	17.6
Mg - 1% Ca in the initial state, Fe-18W-4Cr-0.8C indenter (HA on the contact surfaces) **(2)**	693	73.4	0.11	0.07	13.2
Mg - 1% Ca after ECAP, Fe-18W-4Cr-0.8C indenter (contact surfaces are degreased) **(3)**	785	88.7	0.11	0.1	11.4
Mg - 1% Ca after ECAP, Fe-18W-4Cr-0.8C indenter (HA on the contact surfaces) **(4)**	785	55.2	0.07	0.07	0.7
Mg - 1% Ca after HPT, Fe-18W-4Cr-0.8C indenter (contact surfaces are degreased) **(5)**	564	62.4	0.11	0.1	9.1
Mg - 1% Ca after HPT, Fe-18W-4Cr-0.8C indenter (HA on the contact surfaces) **(6)**	540	49.9	0.09	0.07	12.2

β^* is the strengthening coefficient of molecular bonds under compressive stresses;

τ_0^* is the shear strength of adhesive bonds in the absence of normal loading

It can be seen from the table that the smallest values of the strength of adhesive bonds and the adhesive component of the friction coefficient are observed for samples processed by HPT in the presence of a bone tissue simulator in the form of hydroxyapatite suspension on the contact surfaces. This may be related to the fact that despite the post-processing annealing after HPT processing and some grain size growth, the high strength of the investigated material is preserved [13]. In addition, this may be due to the lubricating effect of HA which provides the creation of an intermediate "third body" [29]. This is confirmed by the results of the tribological tests for the samples in the initial state and after SPD processing by HPT and ECAP with the use of hydroxyapatite.

5. CONCLUSIONS:

1. The performed research demonstrates a high efficiency of increasing the strength of the Mg-1%Ca magnesium alloy by deformation treatment. The SPD processing by ECAP and HPT reduced the mean grain size from originally 100 μm to 4 μm and 1,4 μm, respectively, which had an effect on the tribological behavior of the examined conjugations.
2. With decreasing grain size, the values of the shear strength of adhesive bonds and the adhesive component of the friction coefficient also decreased, by 9% after ECAP processing and by 35% after HPT. The adhesive component of the friction coefficient decreased by about 18% after both types of deformation treatment.
3. Bone tissue simulator (hydroxyapatite) applied onto the contact surfaces in the initial state enables reducing the shear strength of adhesive bonds and the adhesive component of the friction coefficient by 24%. After ECAP processing the shear strength of adhesive bonds decreased by 37%, and after HPT processing – by about 18%.
4. Based on the performed research, it was established that the Mg-1%Ca magnesium alloy can be used as a material for an implant that contacts bone tissue.

Acknowledgments: The authors thank the Russian Foundation for Basic Research for the financial support under project No. 20-58-S52001 and the Ministry of Science and Technology, Taiwan, for the financial support under Grant No. MOST 109-2221-E-002-116.

REFERENCES

1. I.A. Khlusov, D.V. Mitrichenko, A.B. Prosolov, O.O. Nikolaeva, G.B. Slepchenko, Yu.P. Sharkeev, *Short review of the biomedical properties and application of magnesium alloys for bone tissue bioengineering*, Bulletin of Siberian Medicine. 2019; 18 (2): 274–286. DOI:10.20538/1682-0363-2019-2-274-286
2. F. Witte, *The history of biodegradable magnesium implants: A review*, Acta Biomater. 2010; 6 (5): 1680–1692. doi:10.1016/j.actbio.2010.02.028
3. R.Z. Valiev, Y. Estrin, Z. Horita, T.G. Langdon, M.J. Zehetbauer, Y.T. Zhu, *Producing bulk ultrafine-grained materials by severe plastic deformation*, JOM: the journal of the Minerals, Metals & Materials Society 58(4): pp 33-39//2006. DOI:10.1007/s11837-006-0213-7
4. T.C. Lowe and R.Z. Valiev, *The use of severe plastic deformation techniques in grain refinement*, JOM: 56(10): pp. 64-68//2004. https://doi.org/ 10.1007/s11837-004-0295-z
5. B. Stalin, V. S. Vidhya, M. Ravichandran, A. Naresh Kumar, G.T. Sudha, *Characterization and Properties of Mg–TiO_2 Composites Produced via Ball Milling and Powder Metallurgy*, Metallofiz. Noveishie Tekhnol., 42, No. 4: 497–509 (2020), DOI:10.15407/mfint.42.04.0497.
6. S. Manivannan, J. Vairamuthu, Samuel Tilahun, M. D. Vijayakumar, C. Ramesh Kannan and B. Stalin, *The influence of rare earth cerium addition on mechanical and corrosion properties cast Mg-6Al-1Zn magnesium alloy*//2020 IOP Conf. Ser.: Mater. Sci. Eng. 988 012111. https://doi.org/ 10.1088/1757-899X/988/1/012111
7. B. Stalin, M. Ravichandran, V. Mohanavel, L.P. Raj, *Investigations on microstructure and mechanical properties of Mg-5wt.% Cu-TiB_2 composites produced via powder metallurgy route*, Journal of Mining and Metallurgy, Section B: Metallurgy 2020 Vol. 56, Issue 1, pp. 99-108. https://doi.org/10.2298/JMMB190315047S
8. J Vairamuthu, S. Tilahun, M.D. Vijayakumar, C. R. Kannan, S. Manivannan and B. Stalin, *The squeeze casting parametric effect on magnesium metal matrix composite*, 2020 IOP Conf. Ser.: Ma-

ter. Sci. Eng. 988 012112 https://doi.org/10.1088/1757-899X/988/1/012112
9. V.M. Chornyi, *The prospects of using biodegradable magnesium-based alloys in osteosynthesis*, Zaporozhskii Meditsinskii Zhurnal. 2013; 6 (81): 76–79 (in Russian).
10. A.Yu. Vinogradov, E.V. Vasiliev, M.L. Linderov, D.L. Merson, E.O. Rzhevskaya, *The effect of equal-channel angular pressing on the structure and mechanical properties of Mg-Zn-Ca magnesium alloy*, Science Vector of Togliatti State University. 2015. № 4 (34), p. 18-24 (in Russian).
11. R.Z. Valiev, *Design of nanostructured metals and alloys with unique properties using severe plastic deformation*, Rossiiskie Nanotekhnologii. – 2006, V.1, №1-2, p. 208-216 (in Russian).
12. R.Z. Valiev, A.P. Zhilyaev, T.G. Langdon, *Bulk Nanostructured Materials: Fundamentals and Applications*, 2014 by John Wiley & Sons, Inc., 456 pages. DOI:10.1002/9781118742679
13. O. Kulyasova, R. Islamgaliev, H.-C. Lin, H. Yılmazer, Microstructure and Mechanical Properties of the UFG Magnesium Alloy Mg-1%Ca, Materials Science Forum. 2020. V. 1016, pp 768-773. DOI: 10.4028/www.scientific. net/MSF.1016.768
14. F. Živić, N. Grujović, G. Manivasagam, C. Richard, J. Landoulsi, V. Petrović, *The Potential of Magnesium Alloys as Bioabsorbable /Biodegradable Implants for Biomedical Applications*//Tribology in Industry, Vol. 36, No. 1 (2014) 67-73.
15. S.-J. Huang, Y.-R. Jeng, V. I. Semenov and Y.-Z. Dai, *Particle Size Effects of Silicon Carbide on Wear Behavior of SiC_p-Reinforced Magnesium Matrix Composites*, Tribology Letters (2011), V. 42, No. 1, p. 79-87. https://doi.org/10.1007/ s11249-011-9751-4
16. V.I. Semenov, L.Sh. Shuster, C.V. Chertovskikh, Y.-R. Jeng, S.-J. Huang, Y.-Zh. Dao, S.-J. Hwang *Tribology of Composite Materials on the Basis of Magnesium Alloy with Powder Filler of SiC*, Tribology in Industry, Volume 29, No. 1&2, 2007, p. 37-40.
17. V.I. Semenov, Y.-R. Jeng, S.-J. Huang, Y.-Zh. Dao, S.-J. Hwang, L.Sh. Shuster, S.V. Chertovskikh and P.-Ch. Lin, *Tribological properties of the AZ91D magnesium alloy hardened with silicon carbide and by severe plastic deformation*, Journal of Friction and Wear. Vol. 30, (2009), pp. 194–198
18. Y.D Liao, Z.Y Li, G.Q Tang. *Evaluation for adhesion strength of coating and substrate by burying beforehand specimen*, Journal of Wuhan University of Technology-Mater Sci Ed Vol. 18, (2003), pp. 31-35.
19. S.A. Lurie, P.A. Belov, D.B. Volkov-Bogorodsky, *Multiscale modeling in the mechanics of materials: cohesion, interfacial interactions, inclusions and defects*, in book: Lecture Notes in Applied and Computational Mechanics–Analysis and Simulation of Multield Problems, vol. 12, Springer, 2003 DOI:10.1007/978-3-540-36527-3_9
20. Y. Ichikawa, S. Barradas, F. Borit, V. Guipont, M. Jeandin, M. Nivard, L. Berthe, K. Ogawa, T. Shoji, *Evaluation of Adhesive Strength of Thermal-Sprayed Hydroxyapatite Coatings Using the LAser Shock Adhesion Test (LASAT)*, Materials Transactions, Vol. 48, No. 4 (2007) pp. 793-798. DOI.org/10.2320/matertrans.48.793
21. Y. Zheng, *Magnesium Alloys as Degradable Biomaterials*, CRC Press, 2015, 578 p. DOI:10.1201/b18932
22. L.Sh. Shuster *Adhesive Interaction Between Solid Metallic Bodies*, Ufa: Gilem, ISBN 5-7501-0147-9, 1999, 198 p. (in Russian).
23. J.F. Nie, *Precipitation and Hardening in Magnesium Alloys*, Metall Mater Trans A 43, 3891–3939 (2012). DOI:10.1007/s11661-012-1217-2.
24. K. Oh-ishi, R. Watanabe, C.L. Mendis, K. Hono, *Age-hardening response of Mg–0.3 at.%Ca alloys with different Zn contents*, Materials Science and Engineering (2009) A 526(1) p.177-184 DOI:10.1016/j.msea.2009.07.027
25. E.V. Vasilev, V.I. Kopylov, M.L. Linderov, A.I. Brilevsky, D.L. Merson, A.Yu. Vinogradov, *High strength and fatigue properties of Mg-Zn-Ca alloys after severe plastic deformation*, Letters on Materials. 9(2) (2019), pp 157-161. https://doi.org/10.22226/2410-3535-2019-2-157-161
26. S.V. Dobatkin, E.A. Lukyanova, N.S. Martynenko, N.Yu. Anisimova, M.V. Kiselevskiy, M.V Gorshenkov, N.Yu. Yurchenko, G.I. Raab, V.S. Yusupov, N. Birbilis, G.A. Salishchev and Y.Z. Estrin, *Strength, corrosion resistance, and biocompatibility of ultrafine-grained Mg alloys after different modes of severe plastic deformation*, IOP Conf. Ser.: Mat. Sci. Eng. 194 (2017) 012004. DOI:10.1088/1757-899X/194/1/012004
27. W. Li, X. Liu, Y. Zheng, W. Wang, W. Qiao, K.W.K. Yeung, K.M.C. Cheung, S. Guan, O.B. Kulyasova, R.Z. Valiev, *In vitro and in vivo studies on ultrafine-grained biodegradable pure Mg, Mg-Ca alloy and Mg-Sr alloy processed by high-pressure torsion*, Biomaterials Science. V.8, I.18, p. 5071-5087. DOI:10.1039/d0bm00805b
28. F.S. Novik, Ya.B. Arsov, *Optimization of Metal Technology Processes by Experiment Design*, Moscow: Mashinostroenie, 1980. 304 p. (in Russian).
29. I.V. Kragelskiy, *Friction and Wear*, Moscow: Mashinostroenie, 1968. 480 p. (in Russian).

Recent developments and regulations in fire resistance of wood and wood-based composites

Nadir Ayrilmis
Department of Wood Mechanics and Technology, Forestry Faculty, Istanbul University-Cerrahpasa, Bahcekoy, Sariyer, 34473, Istanbul, Turkey
nadiray@istanbul.edu.tr

Abstract: This study focused on the fire-retardant treatment of wood and wood-based composites using various methods. The recent developments in the fire-retardant standards and classification of wood and wood-based composites were reviewed. Most commonly used fire-retardants and commercial application methods of fire retardants such as boron compounds and phosphates to improve fire resistance of wood and wood based composites were explained. Furthermore, fire-retardant mechanism was informed. Novel nanomaterials used in the fire resistance of wood and wood-based composites were introduced. Significant criteria in choosing of the suitable fire retardants for wood and wood-based composites were explained.
KEYWORDS: *FIRE, FLAME RETARDANCY, WOOD, FIRE RETARDANTS, COMBUSTION, WOOD-BASED COMPOSI T*

1. Introduction

Fire resistance is one of the main obstacles to use wood and wood-based composites in structural applications in most countries. In figures, fires in dwellings cause in Europe over 4.000 deaths and 80.000 diverse injuries per year. The cause of death is suffocation due to smoke in about two thirds of the cases, while burns result only in about one third of the fatalities [1].

Fire retardants protect wood against to the fire in different ways [2]:

Promotion of char formation,

- Conversion of volatile gases to inert gases such as water vapour and carbon dioxide,
- Dilution of pyrolysis gases,
- Inhibiting chain reactions of burning in the gas phase,
- Protecting the surface by an insulating/intumescent layer.

Significant criteria in choosing of the suitable fire retardants are as follows:

Low-toxicity to human health
Minimal risk to atmosphere, climate and environment
Flame spread of 25 or less or «Class B»
Self extinguishing
Won't spread fire
Reduced heat release rate
Disrupts volatile gases
Suitable with manufacturing process conditions (resin blending and hot pressing) during production of wood based-composites
Minimum effect on mechanical properties of wood and wood based materials
Easy-suppy
Low-cost
Easy preparation and application to wood and wood-based panels
Type of wood based substrate
Regulatory requirement to be satisfied
New build or maintenance/upgrade
Service life conditions/environment
Installation conditions
Maintenance requirements

2. Fire-retardant treatment methods of wood and wood-based composites

Fire retardants, if correctly applied, provide added value to wood materials extend the market potential of the world's most natural building material.

Commercial applications of fire retardants to wood can be divided to three classes:

1) Impregnation of wood with a fire retardant using vacuum and over pressure.
2) Addition of a fire retardant as a surface application.
3) Addition of a fire retardant to wood during its manufacturing process (in particular adhesive with fire retardant). Compatibility between resin and fire retardant (in terms of acidity of the fire retardant) and hot pressing conditions is significant factor.

Other techniques to improve fire resistance of wood and wood based composites are as follows:

a) Chemical modification

The most common fire retarding chemicals used for wood and wood-based panels are inorganic salts, such as ammonium polyphosphate, monoammonium phosphate, diammonium phosphate, ammonium sulfate, melamine phosphate, guanyl phosphate, ammonium sulphate; aluminum trihydrate (the most widely used fire retardant in the U.S.), magnesium hydroxide, and boron compounds, such as borax, boric acid, borax pentahydrate, disodium octaborate tetrahydrate, ammonium pentaborate, zinc-borate, and zinc chloride [3,4]. Waterborne inorganic salts may be hygroscopic and cause to the corrosion metal fixtures in treated wood.

Chemical mechanisms are often accompanied by one or several physical mechanisms, most commonly endothermic dissociation or dilution of fuel. Charring is the most common condensed phase mechanism (Fig. 1).

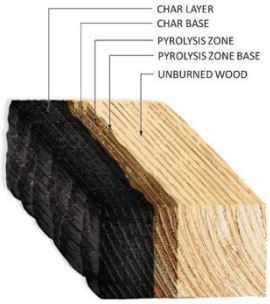

Figure 1. *Superficial carbonization structure of wood exposed to the fire [5].*

b) Physical modification

The physical modifications can include, for instance, combinations of different wood species, methods for higher surface densities, and composites [2]. If the top layer of a wood material consists of a specific species of wood with a relatively low heat release, the heat release peak is smaller, offering possibilities to improve the reaction-to-fire class of the wood material. Alternatively, fire-retardant treated lamellas can be included in wood as surface layers. Using this method, the consumption of fire retardant is reduced compared to wood materials that are fire-retardant treated as a whole. Ignition can be delayed by introducing a high-density surface layer on a wood material. High pressure laminate, for example, might be used for this purpose [2].

c) Nanocomposites

Fire performance of wood and wood-based composites can be improved by using nanocomposites made of layered silicates and

organic polymers. The mechanism of fire retardancy of nanocomposites is generally considered to be due to the structure of the char formed during combustion, which enables the char to thermally insulate the polymer and inhibit the formation and escape of volatiles. Nanoscale fire retardants, such as SiO_2, TiO_2 and ZrO_2, nanoclay, nano-wollastonite, carbon nanotube, nano-silica, have a high ratio of surface area to weight; the smaller the particle size is, the bigger the ratio of surface area to weight. These adavantages improve fire resistance of nanoscale fire retardant chemicals. In addition, nanoscale fire retardants, for example zinc borate, can adsorb more smoke and dust per unit weight than regular sizes during wood combustion.

The most commonly used test methods and guidance documents for the reaction to fire testing of wood materials are as follows:

1. Non-combustibility test EN ISO 1182
2. Gross calorific potential test EN ISO 1716
3. Single Burning Item test EN 13823
4. Ignitability test EN ISO 11925-2
5. Radiant panel test EN ISO 9239-1

3. Fire protection classes of wood materials

Fire protection classes of the materials according to EN 13501-2 and DIN 4102 is given in Table 1. According to Table 1, for example, F90 means that escape routes beneath the fire are protected for up to 90 minutes.

Table 1. *Fire protection classes of the materials.*

Test designation type	Fire protection class		Fire protection in min.
	EN 13501-2	DIN 4102	
fire retarding	REI 30	F 30	30
highly retardent	REI 60	F 60	60
fire resisting	REI 90	F 90	90
fire resisting	REI 120	F 120	120
high fire resistance	REI 180	F 180	180

The relevant classification system is based on the EN 13501-1. In the Euroclass system, building materials are divided to seven classes on the basis of their reaction-to-fire properties. The performance description and the fire scenario for each class are presented in Table 2 according to the main principles used in the development of the Euroclass system [2].

Table 2. Indicative performance descriptions and fire scenarios for Euro-classes.

Class	Performance description	Fire scenario and heat attack		Examples of products
A1	No contribution to fire	Fully developed fire in a room	At least 60 kW/m^2	Products of natural stone, concrete, bricks, ceramic, glass, steel and many metallic products
A2	"	"	"	Products similar to those of class A1, including small amounts of organic compounds
B	Very limited contribution to fire	Single burning item in a room	40 kW/m^2 on a limited area	Gypsum boards with different (thin) surface linings Fire retardant wood products
C	Limited contribution to fire	"	"	Phenolic foam, gypsum boards with different surface linings (thicker than in class B)
D	Acceptable contribution to fire	"	"	Wood products with thickness ≥ about 10 mm and density ≥ about 400 kg/m^3 (depending on end use)
E	"	Small flame attack	Flame height of 20 mm	Low density fibreboard, plastic based insulation products
F	No performance requirements	–	–	Products not tested (no requirements)

The highest possible European class for fire retardant wood materials is class B. Untreated wood usually fulfils class D. The main parameters influencing the reaction to fire characteristics of all wood are product thickness, density and end use conditions such as substrates or air gaps behind the wood material [6].

Table 3. *Classification of wood and wood-based composites according to EN 13986 standard.*

Wood-based panel products[2)]	EN product grade reference	Minimum density (kg/m^3)	Minimum thickness (mm)	Class[3)] (excluding floorings)	Class[4)] Floorings
Particleboards	EN 312	600	9	D-s2, d0	D_{FL}-s1
Fibreboards, Hard	EN 622-2	900	6	D-s2, d0	D_{FL}-s1
Fibreboards,	EN 622-3	600	9	D-s2, d0	D_{FL}-s1
Medium		400	9	E, pass	E_{FL}
Fibreboards, Soft	EN 622-4	250	9	E, pass	E_{FL}
Fibreboards, MDF[5)]	EN 622-5	600	9	D-s2, d0	D_{FL}-s1
Cement-bonded particleboard[6)]	EN 634-2	1000	10	B-s1, d0	B_{FL}-s1
OSB board[7)]	EN 300	600	9	D-s2, d2	D_{FL}-s1
Plywood	EN 636	400	9	D-s2, d0	D_{FL}-s1
Solid wood panels	EN 13353	400	12	D-s2, d0	D_{FL}-s1

1) EN 13986
2) Wood-based panels mounted without an air gap directly against class A1 or A2-s1,d0 products with minimum density 10 kg/m^3 or at least class D-s2,d0 products with minimum density 400 kg/m^3
3) Class as provided for in Table 1 of the Annex to Commission Decision 2000/147/EC
4) Class as provided for in Table 2 of the Annex to Commission Decision 2000/147/EC
5) Dry process fibreboard
6) Cement content at least 75% by mass
7) Oriented strand board

Structural timber with minimum mean density of 350 kg/m^3 and minimum thickness and width of 22 mm may, based on the evidence presented, be classified without further testing as class D-s2, d0. Glued laminated timber (Glulam) with minimum mean density of 380 kg/m^3 and minimum thickness and width of 40 mm can be classified without further testing as class D-s2, d0 [6]. Classes of reaction to fire performance for construction materials excluding floorings are given in Table 4 [2]. The significant parameters affecting the reaction to fire behavior of wood material are its density and thickness, and final use conditions such as substrates or air gaps behind the wood material. For wood materials except floorings the relevant main classes are B, C, D, and E. The relevant additional classes for smoke development are s1, s2 and s3, and for burning droplets d0, d1 and d2 (Table 4).

Table 4. *Euroclass of reaction to fire performance for construction materials excluding floorings [2].*

Class	Test method(s)	Classification criteria	Additional classification
A1	EN ISO 1182 (1); *and*	$\Delta T \le 30°C$; *and* $\Delta m \le 50\%$; *and* $t_f = 0$ (i.e. no sustained flaming)	-
	EN ISO 1716	PCS ≤ 2.0 MJ.kg^{-1} (1); *and* PCS ≤ 2.0 MJ.kg^{-1} (2) (2a); *and* PCS ≤ 1.4 MJ.m^{-2} (3); *and* PCS ≤ 2.0 MJ.kg^{-1} (4)	
A2	EN ISO 1182 (1); *or*	$\Delta T \le 50°C$; *and* $\Delta m \le 50\%$; *and* $t_f \le 20s$	
	EN ISO 1716; *and*	PCS ≤ 3.0 MJ.kg^{-1} (1); *and* PCS ≤ 4.0 MJ.m^{-2} (2); *and* PCS ≤ 4.0 MJ.m^{-2} (3); *and* PCS ≤ 3.0 MJ.kg^{-1} (4)	
	EN 13823 (SBI)	FIGRA ≤ 120 W.s^{-1}; *and* LFS < edge of specimen; *and* $THR_{600s} \le 7.5$ MJ	Smoke production(5); *and* Flaming droplets/ particles (6)
B	EN 13823 (SBI); *and*	FIGRA ≤ 120 W.s^{-1}; *and* LFS < edge of specimen; *and* $THR_{600s} \le 7.5$ MJ	Smoke production(5); *and* Flaming droplets/ particles (6)
	EN ISO 11925-2(8): *Exposure = 30s*	Fs ≤ 150mm within 60s	
C	EN 13823 (SBI); *and*	FIGRA ≤ 250 W.s^{-1}; *and* LFS < edge of specimen; *and* $THR_{600s} \le 15$ MJ	Smoke production(5); *and* Flaming droplets/ particles (6)
	EN ISO 11925-2(8): *Exposure = 30s*	Fs ≤ 150mm within 60s	
D	EN 13823 (SBI); *and*	FIGRA ≤ 750 W.s^{-1}	Smoke production(5); *and* Flaming droplets/ particles (6)
	EN ISO 11925-2(8): *Exposure = 30s*	Fs ≤ 150mm within 60s	
E	EN ISO 11925-2(8): *Exposure = 15s*	Fs ≤ 150mm within 20s	Flaming droplets/ particles (7)
F	No performance determined		

(1) For homogeneous products and substantial components of non-homogeneous products.
(2) For any external non-substantial component of non-homogeneous products.
(2a) Alternatively, any external non-substantial component having a PCS ≤ 2.0 MJ/m^2, provided that the product satisfies the following criteria of EN xxxx(SBI) : FIGRA ≤ 20 W.s^{-1}; *and* LFS < edge of specimen; *and* $THR_{600s} \le 4.0$ MJ; *and* s1; *and* d0.
(3) For any internal non-substantial component of non-homogeneous products.
(4) For the product as a whole.
(5) **s1** = SMOGRA ≤ 30m^2.s^{-2} *and* $TSP_{600s} \le 50$m^2 ; **s2** = SMOGRA ≤ 180m^2.s^{-2} *and* $TSP_{600s} \le 200$m^2; **s3** = not s1 or s2.
(6) **d0** = No flaming droplets/ particles in ENxxxx (SBI) within 600s; **d1** = No flaming droplets/ particles persisting longer than 10s in ENxxxx (SBI) within 600s; **d2** = not d0 or d1; Ignition of the paper in EN ISO 11925-2 results in a d2 classification.
(7) Pass = no ignition of the paper (no classification); Fail = ignition of the paper (**d2** classification).
(8) Under conditions of surface flame attack and, if appropriate to the end–use application of the product, edge flame attack.

4. Conclusions

When the wood is heated, it burns by producing flammable volatiles that can ignite. To reduce combustion, wood is treated with fire retardants which significantly decrease the rate at which flames travel across the wood surface. Nevertheless, some fire-retardant treatments may produce unwanted secondary side effects, for example, increased moisture content, reduced strength and increased potential to corrode metal connectors. To decrease these negative effects, fire retardant treatments may improve the fire performance of wood and wood-based composites considerably through reducing ignitability, rate of heat release and flame spread. This study summarized the fire-retardant treatment mechanism, national and international fire testing standards, and commonly used fire retardants in wood industry. When the wood is protected against to the fire using fire-retardants, its use will increase in construction industry, especially for structural timbers as well as home furniture, doors, window frames, and other applications.

5. References

[1] Anonymous. European Project. FP7-SME-2012-1-315425. Flame-retardant coatings based on nano-magnesium hydroxide, huntite and hydromagnesite for wood applications, wood-Flaretcoat, 2015.

[2] Anonymous. Innovative eco-efficient high fire performance wood products for demanding applications. Material related to the Project. 2015 [http://virtual.vtt.fi/virtual/innofirewood/].

[3] Anonymous. Flame retardants under fire. 2015 [https://www2.buildinggreen.com/article/flame-retardants-under-fire].

[4] Ayrilmis, N., Kartal, S.N., Laufenberg, T., Winandy, J.E., White, R.H. Physical and mechanical properties and fire, decay, and termite resistance of treated oriented strandboard. Forest Products Journal 2015;55(5):74-81.

[5] Le, T.D.H., Tsai, M.T. Experimental assessment of the fire resistance mechanisms of timber-steel composites. Materials 2019;12:4003.

[6] Ostman, B.A.L., Mikkola, E. European classes for the reaction to fire performance of wood products. Holz als Roh- und Werkstoff 2006;64:327-337.